12-2019

Development and Testing of a Hydrogen Peroxide Injected Thrust Augmenting Nozzle for a Hybrid Rocket

Mark C. Heiner
Utah State University

DEVELOPMENT AND TESTING OF A HYDROGEN PEROXIDE INJECTED THRUST AUGMENTING NOZZLE FOR A HYBRID ROCKET

by

Mark C. Heiner

A thesis submitted in partial fulfillment
of the requirements for the degree

of

MASTER OF SCIENCE

in

Aerospace Engineering

Approved:

Stephen Whitmore, Ph.D. Major Professor	David Geller, Ph.D. Committee Member
Geordie Richards, Ph.D. Committee Member	Richard S. Inouye, Ph.D. Vice Provost for Graduate Studies

UTAH STATE UNIVERSITY
Logan, Utah

2019

ABSTRACT

Development and Testing of a Hydrogen Peroxide Injected Thrust Augmenting Nozzle for a Hybrid Rocket

by

Mark C. Heiner, Master of Science

Utah State University, 2019

Major Professor: Stephen A. Whitmore, Ph.D.
Department: Mechanical and Aerospace Engineering

A Thrust Augmenting Nozzle (TAN) using hydrogen peroxide as secondarily injected propellant has been built and tested. The system operates by injecting hydrogen peroxide into the hybrid rocket supersonic core flow downstream of the nozzle throat. This increases the enthalpy and internal pressure of the core flow. This phenomenon can be used with an over-expanded nozzle to act as an altitude-compensating nozzle. By increasing the internal pressure, thrust losses due to over expansion of core flow gases is mitigated. Using secondary injection, the thrust of an over-expanded nozzle was increased by 4%. Significant losses were experienced due to inadequate dwell time of the supersonic flow in the nozzle. Using chemical kinetics and generalized compressible flow theory, a computer model was developed to investigate the losses. It was found that less than 30% of peroxide injected into the nozzle had time to vaporize and react with the core flow gases. It was determined that by increasing the nozzle length by four times the dwell

time would theoretically be sufficient to vaporize all peroxide if the injected peroxide was sufficiently atomized. Optimal configuration of the thrust augmenting nozzle was also explored. With further testing to allow for adequate dwell time and to validate the computer model, it is expected that the TAN system using hydrogen peroxide would greatly increase the payload capacity of a single stage to orbit launch vehicle.

(97 pages)

PUBLIC ABSTRACT

Development and Testing of a Hydrogen Peroxide Injected Thrust Augmenting Nozzle for a Hybrid Rocket

Mark C. Heiner

During a rocket launch, the point at which the most thrust is needed is at lift-off where the rocket is the heaviest since it is full of propellant. Unfortunately, this is also the point at which rocket engines perform the most poorly due to the relatively high atmospheric pressure at sea level. The Thrust Augmenting Nozzle (TAN) investigated in this paper provides a solution to this dilemma. By injecting extra propellant into the nozzle but downstream of the throat, the internal nozzle pressure is raised and the thrust is increased, and the nozzle efficiency, or specific impulse is potentially improved as well. Using this concept, the payload capacity of a launch vehicle can be increased and provides an excellent option for single stage to orbit vehicles.

ACKNOWLEDGMENTS

I would like to thank Dr. Stephen Whitmore for his guidance and support throughout the entire research and testing process. He was patient through my shortcomings and generous with his advice.

Thank you to the machinists, Keith Covert, for generously donating his labor and material to building the thrust augmenting nozzle, and to Terry Zollinger, who repaired and remade the nozzle multiple times.

Thank you to my fellow graduate students, Isaac Armstrong, Evan Zelesnik, Rob Stoddard, and Tyler Gardner, who helped with building, testing, and rebuilding.

Finally, I give special thanks to my family, who supported me all along the way and never gave up hope. They shouldered my trials with me and endured my absence through what seemed at times to be a futile effort. There were times that things seemed grim, but they never lost the faith. I could not have completed my thesis without their patience and support.

Mark C. Heiner

CONTENTS

Page

LIST OF TABLES

LIST OF FIGURES

Figure Page

Figure Page

ACRONYMS

ABS	acrylonitrile butadiene styrene
CEA	Chemical Equilibrium with Applications
CFD	computational fluid dynamics
GOX	gaseous oxygen
H_2O_2	hydrogen peroxide
HDPE	high-density polyethylene
HIPS	high-impact polystyrene
HTP	high-test peroxide
HTPB	hydroxyl-terminated polybutadiene
LDPE	low-density polyethylene
NASA	National Aeronautics and Space Administration
NTR	nuclear thermal rocket
P&ID	piping and instrumentation diagram
TAN	thrust augmenting nozzle
USU	Utah State University

NOMENCLATURE

A	nozzle cross-sectional area
A_{inj}	nozzle cross sectional area at injector site
A_0	pre-exponential or frequency factor
A_1	*v*enturi inlet area
A_2	venturi outlet area
A^*	nozzle cross sectional area at which local flow chokes
C_d	discharge coefficient
C_F	thrust coefficient
C^*	effective exhaust velocity
D	droplet diameter
D_{AB}	bianary diffusivity
E_a	activation energy
F	thrust
H	enthalpy term
h	specific enthalpy
h_{pr}	constant pressure heat of combustion
I_{sp}	specific impulse
K	Arrhenius reaction rate constant
L_K	Knudsen layer thickness
M	Mach number
M_{hp}	molarity of vaporized hydrogen peroxide solution
m_d	droplet mass
Δm_{fuel}	consumed fuel mass, g
n_d	number of dropletes inside control volume
$\dot{n}_d$	droplet flow rate
O/F	oxidizer/fuel ratio
P	pressure
P_1	venturi inlet pressure
P_2	venturi throat pressure
P_0	core flow stagnation pressure
Pr	Prandtl number
Q	heat transfer rate
R	universal gas constant
Re	Reynolds number
R_g	species gas constant
Sc	Schmidt number
Sh	Sherwood number
T	temperature
T_B	atmospheric boiling point of injectant
T_C	critical temperature of injectant
T_0	stagnation temperature

t	burn time or general time
v	velocity
w	massflow rate
w_r	hydrogen peroxide mass decomposition rate
W	molecular weight
x	longitudinal coordinate
X	drag exerted on suspended droplets
$\mathcal{X}_{s,neq}$	non-equilibrium surface molar fraction
Y_G	far-field vapor mass fraction
$Y_{s,neq}$	non-equilibrium surface mass fraction
β	non-dimensional evaporation parameter
γ	ratio of specific heats
η_{comb}	combustion efficiency
μ	viscosity
ρ	density
τ_d	evaporation time constant
ϕ	equivalence ratio

subscripts

ox	oxidizer property
fuel	fuel property
core	core flow property
g	gas or core flow property
L	injected liquid property
v	unreacted 90% hydrogen peroxide vapor
d	droplet property
exit	exit condition
total	combined core flow and unreacted vapor

CHAPTER 1

INTRODUCTION

Traditionally, high-expansion ratio nozzles have been limited to only in-space operations. Lift-off launch vehicle stages generally require low expansion ratios in order to prevent internal flow separation and embedded shock waves. Consequently, multiple stages with locally optimized nozzles are required to reach orbit, which significantly increases the cost of the launch stack. Saving just one stage in the launch cycle could result in considerable cost savings.

The Thrust Augmented Nozzle (TAN) overcomes conventional limitations by injecting additional propellants downstream of the nozzle throat, resulting in secondary combustion. Downstream burning “fills-up” the nozzle and significantly raises exit pressure. This effect allows an efficient high expansion ratio nozzle to operate at low altitudes without risk of flow field separation.

This thrust increase at sea-level conditions is very beneficial to overall launch vehicle performance. At lift-off conditions, the rocket is at its heaviest due to the large mass ratio of propellant. This is also where gravity losses are most significant. Due to these factors, thrust at lift off must be the highest that the entire launch stack can deliver. Unfortunately, as stated earlier, this is also the point at which nozzles operate the least effectively. Using secondary injection greatly increases lift-off thrust, delivering the added thrust when it’s needed. Thrust augmentation acts as an extra rocket booster without added mass of strap on rocket boosters or extra engines. The thrust augmenting nozzle can significantly increase launch vehicle payload capacity.

The TAN design to be reported retrofits an existing hybrid rocket system burning 90% Hydrogen Peroxide and Acrylonitrile-Butadiene-Styrene (ABS) as propellants, with an embedded a helical fuel port. This helical port, fabricated using 3-D additive manufacturing, significantly increases fuel regression rates, resulting in a fuel-rich combustor exit plume. When peroxide is injected downstream of the throat, the hot unburned hydrocarbons spontaneously ignite, releasing heat from both secondary combustion and thermal decomposition of the peroxide. The secondary peroxide decomposition also produces large volumes of gas that are captured by the nozzle, significantly increasing the exit pressure.

Eleven tests were conducted demonstrating effectiveness of the TAN system with hydrogen peroxide. The results will be analyzed and compared to computer simulations to determine optimal configurations.

1.1 Background

Conventional fixed-geometry rocket nozzles allow optimum performance only at one specific ambient pressure or operating altitude. Thus, conventional nozzles necessarily represent a design compromise. In a conventional nozzle, combustion gases are choked by a cylindrical throat and then expand through a diverging nozzle pathway, exchanging thermal energy for kinetic energy, and creating a large increase in momentum of the exit plume. The optimal operating condition for a conventional nozzle occurs when the pressure at the exit plane exactly equals the background ambient pressure. This condition is set by the chamber pressure and expansion ratio. Figure 1.1 shows the flow fields associated with an over-expanded, optimally-expanded, and under-expanded bell

nozzle [1]. For the conventional nozzle careful design is needed to achieve desired high altitude (under-expanded operating conditions) performance while avoiding flow separation and an embedded shock wave when operating at low altitudes (over-expanded operating conditions).

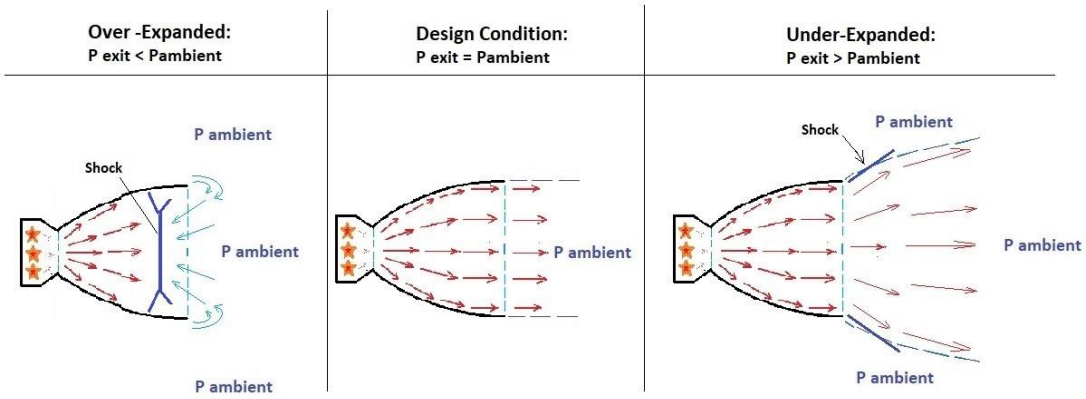

Fig. 1.1 Over-expanded, optimally expanded, and under-expanded flow regimes for a conventional fixed-geometry bell nozzle.

The over-expanded nozzle develops an exit pressure that is less than the surrounding atmospheric pressure, and a locally negative pressure gradient results. When the negative pressure gradient becomes sufficiently strong, boundary layer separation and backflow can form along the nozzle walls. Backflow and flow separation typically result in the formation of an embedded shockwave. The embedded shock wave leads to a loss of performance, and possible structural failure due to high heating levels at the shock-wall interface and dynamic loads due to flow separation.

For under-expanded conditions the nozzle is fully started and isentropic; however, the exit plane pressure is substantially higher than ambient; meaning that the only a portion of the thermal energy of the plume has been recovered and converted into kinetic

energy. The result is the potential for a considerable loss in the available nozzle momentum thrust. Consequently, typically lower expansion ratio nozzles are used for low altitude operation, and high expansion ratio nozzles are reserved for near-space operations. Few designs are able to bridge the gaps between operating altitudes.

1.2 Thrust Augmented Nozzle Concept

The Thrust Augmented Nozzle (TAN) [2] technology researched by this study offers a practical solution for altitude compensation by operating an over expanded nozzle at low altitudes, and then "filling up" the nozzle to match ambient exit pressure, injecting and burning propellant downstream of the throat in the divergent section of the nozzle. By injecting propellant into the divergent section of the over expanded nozzle, the exit pressure is increased and is driven towards the optimal level. The secondary mass flow can be varied based on ambient conditions, making the TAN system a viable operational option. Figure 1.2 illustrates the TAN concept.

Previously TAN systems injected both fuel and oxidizer into the diverging core flow. This process has been demonstrated to give significant gains in performance, increasing the thrust to weight ratio of a 650-klbf-thrust class engine by more than 60% [3]. A primary issue associated with bi-prop TAN systems is that two injection flow paths are required, and these propellants must dwell within the nozzle with sufficient time to allow combustion. Thus, because of the high supersonic flow conditions in the divergent nozzle section, dwell times are limited and tuning the characteristic lengths of the system (L^*) is extremely difficult [4].

To date little work has been done experimentally demonstrating the utility of

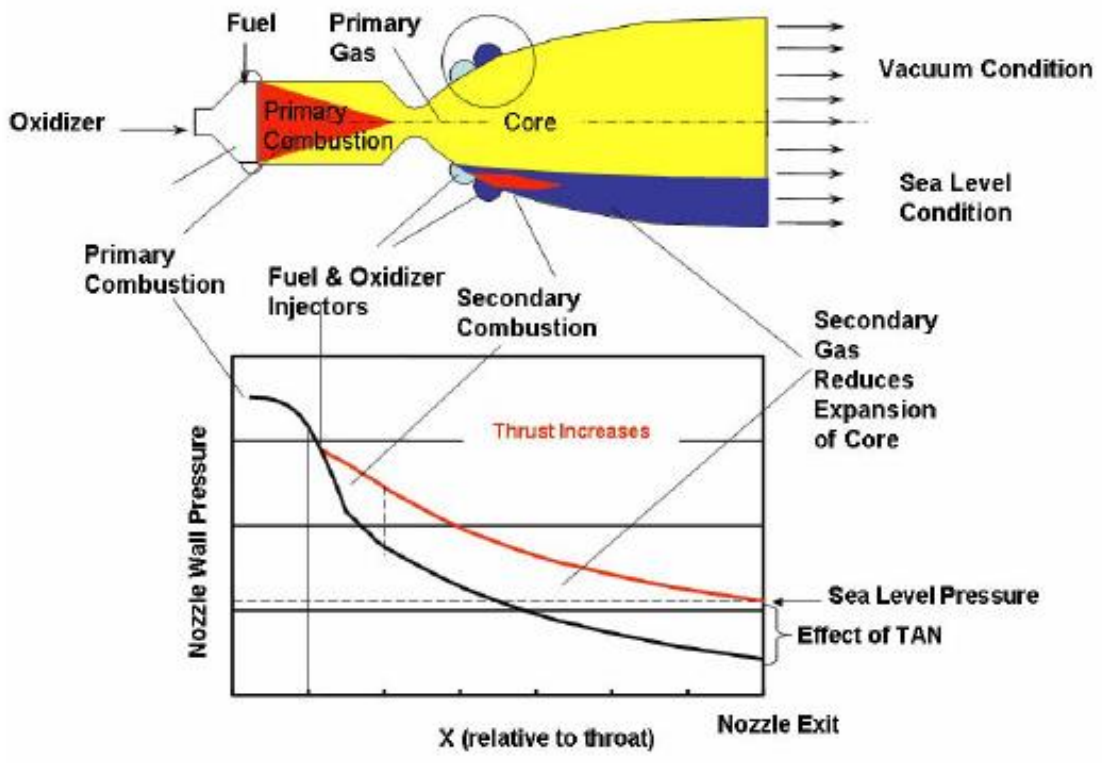

Fig. 1.2 TAN concept as altitude compensating nozzle.

injecting only a single propellant into the nozzle. One early single-propellant injection TAN design was proposed in 1994 by Borowski et al [5] as a way to increase thrust from a nuclear thermal rocket (NTR). The NTR, operated by heating hydrogen gas using a nuclear reactor, offers very high specific impulse levels with relatively low thrust levels. As a way to increase thrust on an as needed basis, liquid oxygen (LOX) could be injected downstream of the throat, combusting the hot hydrogen gas. This concept is very similar to an afterburner on a turbojet, injecting oxidizer into fuel-rich flow instead of injecting fuel into lean exhaust products.

Borowski et. al. investigated injection techniques, suggesting that the most effective way to inject fuel is normal to the flow stream. A trade off exists with injector

angle and TAN efficacy. Zhu et al. [6] performed a computational fluid dynamics (CFD) analysis of injecting fuel into supersonic air at various angles and concluded that penetration and mixing increased with increased or forward pointing injector angle. They also found that the shock angle increases, creating a stronger shock wave and losses in that regard. Borowski et. al. also stressed the importance of not driving the Mach number too low with heat addition to minimize Rayleigh losses, keeping flow in the Mach 1.5 to 2.0 range near the injection site. This concept of Rayleigh losses and the need to stay in the high Mach number regime for smaller entropy losses when combusting in supersonic flow is reinforced by Riggins et al. [7].

1.3 Hybrid Rocket Principles

All results presented in this paper were obtained from static test firings of a hybrid rocket motor. Hybrid rockets possess several qualities that make them a viable alternative to conventional liquid or propellant propulsion systems [8]. The biggest draw to hybrid propulsion systems is the intrinsic safety. Generally, the oxidizer is stored in liquid or gaseous form, while the fuel is stored in solid form. This phase separation of oxidizer and fuel make it more difficult for unintentional detonation to occur. The fuel first needs to be converted to a gaseous state, or pyrolyze, to interact with the oxidizer and for combustion to occur. The relative inertness of the fuel also makes operations such as transportation, storage, loading, and operation safer. These added safety margin significantly reduce operating cost. Hybrid thrusters are also significantly less complex than their liquid propulsion counterparts due to only a single flow path.

Common fuels used for hybrid rockets are typically hydroxyl-terminated

polybutadiene (HTPB) or various paraffin-based fuels. Common oxidizers include nitrous oxide, hydrogen peroxide, and oxygen. Most hybrid rocket fuels and oxidizers are considered “green,” meaning that they present less human and environmental hazards.

The “greenness” of hybrid rockets, along with the higher safety factor and reduced operating cost make it a very obvious choice as a thrust chamber to use with the thrust augmenting nozzle.

1.4 GOX Injected Thrust Augmented Nozzle

Recently, the Propulsion Research Laboratory at Utah State University investigated the feasibility of applying single-propellant secondary injection to a medium-scale hybrid rocket system to practically achieve TAN. The underlying concept was to burn the rocket system fuel rich, and then inject oxidizer downstream into the hot flow field. When the secondary oxidizer is injected into the nozzle downstream of the throat, the hot unburned, pyrolyzed hydrocarbons in the plume spontaneously ignite. Since the associated fuel in the combustion products was already partially decomposed, it was reasoned that such a system would reignite more readily than a bi-prop system. The simplicity of only requiring one secondary injection path was also an added benefit.

The early TAN hybrid system used 3-D printed acrylonitrile butadiene styrene (ABS) plastic as fuel and gaseous oxygen (GOX) as oxidizer and as secondarily injected propellant [9]. While this design was simple and effective, it exhibited some significant shortcomings. Because the stoichiometric oxidizer-to-fuel (O/F) ratio for GOX/ABS is only 2.0, in order to achieve secondary combustion a high proportion of unburned fuel in the combustion chamber outlet products was required.

Early GOX/ABS tests performed using a cylindrical fuel port did not produce a sufficiently-rich combustion chamber flow to allow secondary ignition. In order to lower the O/F ratio the initial design leveraged 3-D additive manufacturing to embed a helical fuel port into the thrust chamber. Previous work by Whitmore et al. [10] demonstrated that an embedded helix can increase the initial fuel regression rate by a factor greater than 5. Thus, the embedded helix was an efficient way to significantly lower the O/F ratio of the combustion chamber exhaust products.

Figure 1.3 shows the GOX/ABS TAN hybrid system in operation. Core flow specific impulse levels were increased significantly. In Fig. 1.3a note that, even though the nozzle is highly over expanded, no shock diamonds are visible. This behavior indicates that the nozzle exit flow is subsonic, and that a strong shock wave is embedded inside of the nozzle. Once secondary injection occurs, the nozzle exit fills in and the plume expands dramatically, indicating significant pressurization of the nozzle exit plane above ambient pressure levels.

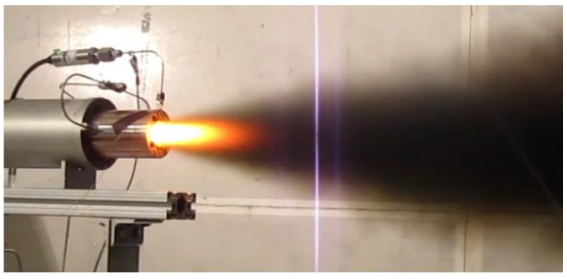

a) Fuel-rich plume exiting high expansion ratio nozzle

b) Fuel rich plume burning after secondary injection

Fig. 1.3 Thrust augmented nozzle with secondary injection burning in high expansion ratio nozzle.

Figure 1.4 shows typical time history results. It plots two time-history traces, one

with secondary injection, and one without secondary injection. Each time history shows two burn pulses. For each time history the motor was initially burned for 15 seconds using a freshly printed helical fuel grain. The motors were subsequently quenched and reignited for an additional 8 seconds. Note that initially the secondary injection motor exhibits a 15% increase in thrust level with no loss in specific impulse due to secondary injection. However, after 10 seconds this advantage drops off, and the second burn exhibits no advantage for the TAN-augmented nozzle.

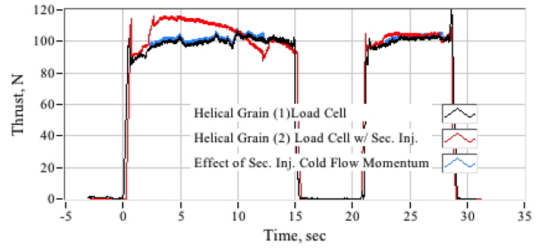

a) Thrust Data for Helical Grains with / without Secondary Injection

a) Thrust data for helical grains with/without secondary injection

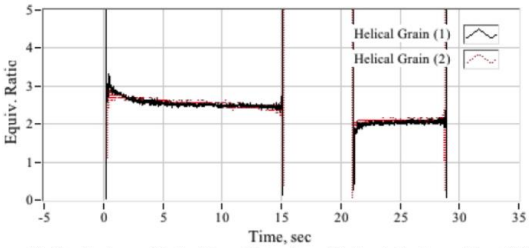

b) Equivalence Ratio Burn Data from Helical Grains of Part (a).

b) Core flow equivalence ratio burn data from grains of part (a)

Fig. 1.4 Effects of equivalence ratio on secondary injection thrust augmentation efficacy.

Note on Fig. 1.4 that the core-flow equivalence ratio Φ—the stoichiometric O/F ratio divided by the actual O/F ratio—is initially very high, greater than 3. Eventually, Φ drops off indicating an increasingly leaner core flow. This drop in equivalence ratio corresponds to the helical port burning away and becoming more and more cylindrical. The drop in Φ corresponds to the resulting drop in fuel regression rate. Control tests performed using cylindrical fuel ports with secondary injection, and helical fuel ports without secondary injection do not exhibit the demonstrated performance increase.

Clearly, both the fuel rich plume and a properly tuned secondary injection are

essential features allowing the hybrid thrust augmentation to occur. Multiple test results reported by Ref. [9] indicate that augmentation only had a positive impact while the fuel port (core flow) equivalence ratio was at least 2.5. Below this value, insufficient fuel vapor was present to allow combustion to occur while the flow was still within the nozzle boundaries. Because the helix erodes away with time, the augmentation effect is always temporary. This result represented a serious limitation for the GOX/ABS TAN hybrid.

Ref. [9] offers are several design geometry changes that could improve results. The immediate solution to this is to use a longer motor. This would increase the equivalence ratio and ideally increase the time during which augmentation would be viable; but at the cost of a volumetrically inefficient motor geometry. Another possible solution offered by Ref. [9] is 3-D printed embedded and buried structures inside the grain that open up as the grain burns, increasing the burn area and equivalence ratio. Another option would be to test even more complex port geometries that maintain a low O/F ratio. The latter two are simple solutions to implement on a 3D printed grain, but would be difficult to optimize.

1.5 Secondary Injection using Hydrogen Peroxide

The research results to be presented leverage the work of Ref. [9] but replace the relatively inert and low specific gravity GOX oxidizer with a significantly denser and more reactive propellant, 90% hydrogen peroxide, H_2O_2. Hydrogen peroxide is not only an efficient oxidizer, but it possesses a powerful decomposition reaction that releases nearly 100 kJ for every mole of peroxide that is decomposed. Figure 1.5 shows the associated end-to-end reaction, neglecting intermediate products. In this concept when

peroxide is injected downstream of the throat, any unburned hydrocarbons will burn with the oxygen released by the thermal decomposition. Thus, heat is derived from both thermal decomposition and secondary combustion of released oxygen with residual fuel in the core flow. The secondary peroxide decomposition also produces large volumes of gas that are captured by the nozzle, and significantly increases the exit pressure. Finally, the stoichiometric *O/F* ratio for 90% H_2O_2 and ABS combustion is approximately 5.5; thus, achieving the desired TAN effect should require a significantly less rich fuel plume. The following two sections detail the design changes required to modify an existing 150 N hybrid system [11] using H_2O_2 and ABS as propellants for TAN Augmentation.

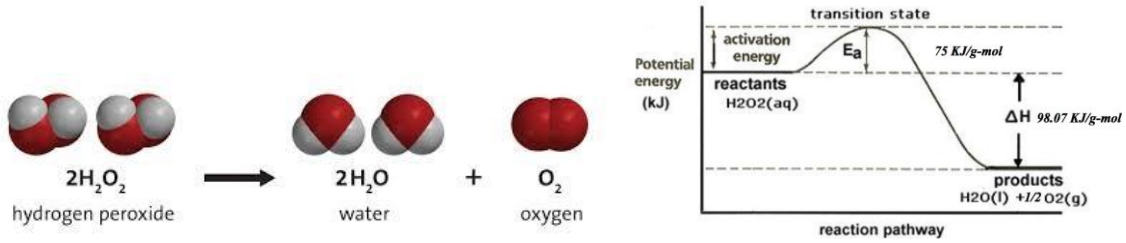

a) Reaction pathway. *b) Peroxide decomposition energy state transition*

Fig. 1.5 Hydrogen peroxide decomposition reaction.

1.6 H2O2/ABS Motor System

The legacy system, previously developed by the USU Propulsion Research Laboratory, leverages a novel, non-catalytic arc-ignition system [12] to thermally decompose the core hydrogen peroxide flow. The arc-ignition technology derives from the electrical breakdown properties of certain 3-D printed thermoplastics like Acrylonitrile Butadiene Styrene (ABS), Low Density Polyethylene (LDPE) and High-Impact-Polystyrene (HIPS). These properties were discovered serendipitously while

investigating the thermodynamic performance of ABS as a hybrid rocket fuel [13]. This arc-ignition concept has been engineered into a power-efficient system that can be started, stopped, and restarted with a high degree of reliability.

In typical rocket applications a heated catalyst bed is used to initiate peroxide decomposition. The catbed lowers the activation energy to the point where a moderate amount of heat can initiate decomposition. Noble metal catalysts like platinum or silver can lower the activation energy to less than 50 kJ/mol. Drawbacks to the catalytic decomposition approach include catalyst poisoning due to the presence of stabilizers in HTP, and susceptibility of the metal catalyst to melting because of the intense heat release. This event renders the use of catalysts not only inconvenient but also quite expensive. Catalyst beds are heavy and contribute nothing to the propulsive mass of the system. Catalytic decomposition typically requires very high concentrations of peroxide, greater than 91%.

These high concentrations of peroxide, greater than 91%, often referred to as HTP, are registered by the US Department of Transportation under the Code of Federal Regulations (CFR) as a Class 4 oxidizer, and as a class 3 unstable material [14]. As a class 4 oxidizer HTP can cause explosive reactions due to contamination or exposure to thermal or physical shock. Additionally, the oxidizer will enhance the burning rate and may cause spontaneous ignition of combustibles. HTP is corrosive and “burns” skin and tissue upon contact. HTP can initiate decomposition of materials which in themselves are not likely to undergo explosive decomposition. HTP is an extremely dangerous material to work with. Storage of significant quantities presents a significant objective hazard.

Using a lower grade class III concentration of peroxide significantly lowers the risks associated with handling and servicing procedures.

An alternative to catalytic decomposition is thermal decomposition. In thermal decomposition no catalyst bed is required and decomposition is achieved by providing sufficient external heat to “get over the hump” of activation energy depicted by Fig. 1.5. Often, HTP thermal decomposition is accompanied by the production of large volume of superheated gas that can lead to explosion. Prior to the methods developed by Whitmore et al. [11] and Whitmore [15], a practical. low-energy thermal ignition system had never been developed.

In this non-catalytic approach, the peroxide flow is pre-lead by a small flow of gaseous oxygen injected into a combustion chamber lined with the 3-D printed ABS fuel. The arc-ignition system weakly initiates combustion between the injected oxygen and the fuel source, and is followed by the peroxide flow. Ref. [15] describes this process in detail. Previous studies have demonstrated that GOX/ABS combustion generates temperatures exceeding 2800^{o}C, and specific enthalpies greater than 8.5 MJ/kg. Thus, with the properly tuned GOX pre-lead mass flow rate, there exists sufficient energy to decompose the incoming peroxide flow, while simultaneously initiating full-length hybrid combustion.

Once peroxide decomposition begins, the additional energy of decomposition contributes to the overall combustion process. After the GOX pre-lead is terminated, combustion is sustained by the oxygen liberated by the thermal decomposition of the peroxide. The arc ignition process is outlined in greater detail in section 3.2. Over 40 tests

have been successfully conducted with this thermal decomposition system at USU, using hydrogen peroxide concentrations as low as 85%.

1.7 H2O2/ABS TAN Motor System

The H_2O_2/ABS system detailed in section above was fitted to a Thrust Augmenting Nozzle and used for this test campaign. The nozzle expansion ratio was increased to a 16:1 area ratio and included two opposing injectors located just downstream of the throat. The design specifics will be laid out in a later chapter. The nozzle was built in a modular fashion to provide easy modification of injector angle and location. Though this thesis will only cover results from using a single configuration of this nozzle, future work with this system may include dispersions of the injector angle and location to explore the effect this would have on performance. For this test campaign, only ignition mechanisms of secondary injection and effects of mass flow on thrust augmentation achieved were tested.

Throughout the course of the test campaign, new findings on use of thermally decomposed hydrogen peroxide in extreme temperature environments were found and will be presented in a later section.

CHAPTER 2

MODELING AND ANALYSIS

This section details the methods that were used to calculate the rocket performance parameters that are to be reported later in CHAPTER 4. Also, an analytical model of the secondary injection, based on influence coefficient methods for quasi-1-dimensional flow, is developed. The model predictions will be compared to the experimental results.

2.1 Determination of Thrust from Chamber Pressure

The purpose of this thesis is to prove the feasibility of a hydrogen peroxide injecting thrust augmenting nozzle as a means of effective altitude compensation. As a point of comparison, a thrust measurement was obtained in two ways. The thrust was measured directly using a load cell, and measured indirectly using the chamber pressure, which was measured using a pressure transducer located by the injector. Using these two independent measurements, the increase in thrust obtained from the secondary injection can be deduced. The load cell measured the actual thrust, and the thrust derived from the chamber pressure measurement reflected the theoretical thrust without the secondary injection. The chamber pressure measurement is independent of secondary injection effects since the nozzle is choked and therefore acting as a barrier for any pressure waves generated from the secondarily injected propellants.

The thrust equation is as follows:

$$F = wv_{exit} + (P_{exit} - P_{\infty})A_{exit} \tag{2.1}$$

Here F is thrust, w is total mass flow rate, v_{exit} is exhaust velocity at the exit plane, P_{exit}

is the exit pressure, P_∞ is the ambient pressure, and A_{exit} is the exit area.

The mass flow rate is calculated using the choking mass flow equation below.

$$w_{core} = \frac{P_0 A^*}{\sqrt{T_0}} \sqrt{\frac{\gamma}{R_g}\left(\frac{2}{\gamma+1}\right)^{\frac{\gamma+1}{\gamma-1}}} \tag{2.2}$$

Here P_0 is the stagnation pressure, T_0 is the stagnation temperature, A^* is the choking area, γ is the specific heat ratio, and R_g is the species gas constant.

Stagnation pressure is measured directly, and A^* is assumed to be the throat area. The rest are strongly correlated with the oxidizer to fuel ratio (O/F) and cannot be measured so must be estimated. They are estimated using NASA's industry standard software Chemical Equilibrium with Applications (CEA) [16]. The propellant species along with O/F ratio and stagnation pressure are input, and the predicted exhaust species are output along with stagnation temperature, species gas constant, and specific heat ratio. The CEA outputs for 90% H_2O_2/ABS are shown in Fig. 2.1.

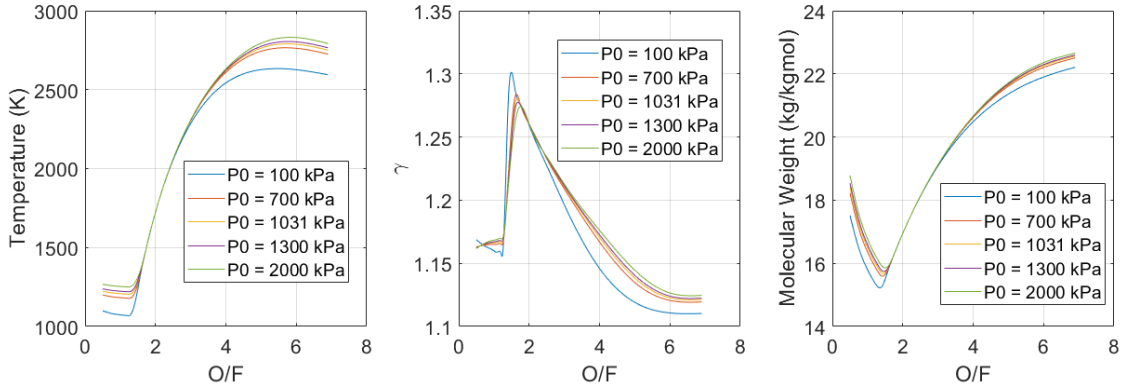

Fig. 2.1 CEA Temperature, specific heat ratio, and molecular weight outputs for 90% H2O2/ABS.

Next, combustion efficiency must be taken into account, which will scale the

actual combustion temperature from the theoretical combustion temperature. Combustion efficiency (η_{comb}) is defined in relation to exhaust velocity, or C^*.

$$C^*_{actual} = \eta_{comb} \cdot C^*_{ideal} \tag{2.3}$$

C^* is defined as follows.

$$C^* = \frac{\sqrt{\gamma R_g T_0}}{\gamma\sqrt{\left(\frac{2}{\gamma+1}\right)^{\frac{\gamma+1}{\gamma-1}}}} \tag{2.4}$$

Assuming that change in γ and R_g due to change in combustion efficiency is negligible, the combustion efficiency can be applied directly to combustion temperature, or stagnation temperature, T_0.

$$T_{0_{actual}} = \eta^2_{comb} \cdot T_{0_{ideal}} \tag{2.5}$$

The exit velocity is determined from exit Mach number (M_{exit}) and the speed of sound.

$$v_{exit} = M_{exit} \cdot c = M_{exit} \cdot \sqrt{\gamma R_g T_{exit}} \tag{2.6}$$

Exit Mach number is found using a numeric solver with the area-Mach number relation.

$$\frac{A}{A^*} = \frac{1}{M}\left[\frac{2}{\gamma+1}\left(1 + \frac{\gamma-1}{2}M^2\right)\right]^{\frac{\gamma+1}{2(\gamma-1)}} \tag{2.7}$$

The exit temperature to find the exit velocity, and the exit pressure can then be determined from the exit Mach number. Finding the exit pressure this way assumes isentropic flow. This assumption will be relaxed later on.

$$\frac{T_0}{T_{exit}} = 1 + \frac{\gamma - 1}{2} M^2 \tag{2.8}$$

$$\frac{P_0}{P_{exit}} = \left(\frac{T_0}{T_{exit}}\right)^{\frac{\gamma}{\gamma-1}} = \left(1 + \frac{\gamma - 1}{2} M^2\right)^{\frac{\gamma}{\gamma-1}} \tag{2.9}$$

The O/F ratio is defined as follows.

$$O/_F = \frac{w_{ox}}{w_{fuel}} \tag{2.10}$$

For all practical purposes, aqueous hydrogen peroxide solutions can be considered to be incompressible. The mass flow rate of the oxidizer, 90% hydrogen peroxide, is determined using a venturi flow meter, and is determined as follows.

$$w_{ox} = A_2 \sqrt{2\rho \frac{P_2 - P_1}{1 - \left(\frac{A_2}{A_1}\right)^2}} \tag{2.11}$$

Here A_1 and A_2 are the inlet and throat area of the venturi, respectively, ρ is the density of the fluid, and P_1 and P_2 are the inlet and throat pressures respectively.

The fuel mass flow rate of a hybrid rocket cannot be measured directly. A before and after measurement of the fuel grain can be taken to determine total change in mass, and this will be used later to help determine combustion efficiency. Since the total mass flow rate is known from the choking mass flow equation, Eq. (2.2), and the oxidizer mass flow is known from Eq. (2.11), the instantaneous fuel mass flow rate ran be taken as the difference between the two.

$$w_{fuel} = w_{total} - w_{ox} \tag{2.12}$$

The total fuel mass consumed was estimated by integrating the calculated mass flow rate of fuel.

$$\Delta m_{fuel} = \int_{t0}^{tf} w_{fuel} \cdot dt \tag{2.13}$$

The calculated change in fuel mass is compared with the measured change in fuel mass. The combustion efficiency and O/F ratio are tweaked until the mass measurements agree. Once the O/F ratio is determined, the thrust is determined through an iterative process as the true O/F ratio is refined to the true value.

2.2 Determination of Combustion Efficiency

As stated before, the combustion properties of $T_0, \gamma, and\ R_g$ are calculated using CEA assuming complete combustion. In reality, there are losses in the combustion chamber due mainly to an incomplete reaction. This non-ideal behavior is accounted for using the combustion efficiency scale factor. The combustion efficiency is an experimentally determined parameter that scales the exhaust velocity and therefore the combustion temperature as well. Adjusting η_{comb} changes the calculated values for fuel mass flow rate, O/F ratio, thrust, and other parameters. The value of η_{comb} is changed until the calculated consumed mass matches the measured change in mass of the fuel grain.

2.3 Thrust Coefficient Increment and Augmentation Ratio

Thrust coefficients will be used to compare the thrust augmentation of burns with and without secondary injection. Thrust coefficient is a unitless quantity that represents the normalized thrust. It is calculated defined as:

$$C_F = \frac{F}{P_0 A^*} \tag{2.14}$$

The effects of thrust augmentation by secondary injection are calculated as the

thrust coefficient increment.

$$\Delta C_F = C_{F,Aug} - C_{F,Base} \tag{2.15}$$

where $C_{F,Aug}$ is the thrust coefficient of a burn that uses secondary injection (augmented), and $C_{F,Base}$ is the thrust coefficient of the baseline (unaugmented) cases. As a point of comparison, all augmented burns will be compared to the average thrust coefficient of all baseline burns. The dimensionless secondary injection mass flow rate or augmentation ratio, AR, is calculated as the ratio of secondary to primary mass flow rates:

$$AR = \frac{w_{si}}{w_{core}} \tag{2.16}$$

Using thrust coefficient increment and augmentation ratio, the thrust response of the system to secondary injection will be characterized.

2.4 Compression Ratio

The compression ratio is the ratio of the pressure at the injector site or the downstream pressure (P_{post}) to the pressure just before the injector, or the upstream pressure (P_{pre}).

$$\text{Compression Ratio} = \frac{P_{post}}{P_{pre}} \tag{2.17}$$

The upstream pressure, P_{pre}, is determined using the isentropic relations for quasi 1-D compressible flow. See Eqs. (2.7) and (2.9). The downstream pressure, P_{post}, is found using the venturi data for mass flow rate. See Eq. (2.11). A secondary means for calculating flow rate is to use the equation for mass flow rate through an orifice.

$$w = C_d A_{inj} \sqrt{2\rho(P_2 - P_1)} \tag{2.18}$$

Here A_{inj} is the injector cross-sectional area, C_d is the injector orifice discharge

coefficient, ρ is the hydrogen peroxide density, and P_1 and P_2 are the pressures before and after the injector, respectively. The discharge coefficient is determined beforehand by calibration using venturi data or by measuring and integrating total throughput. This can be used as a redundant measurement for the main oxidizer mass flow since both the injector pressure, P_1, and the chamber pressure, P_2, are known. However, since the downstream pressure, P_{post} or P_2, is unknown as this point, it can be found by rearranging Eq. (2.18).

$$P_2 = \left(\frac{w}{C_d A_{inj}}\right)^2 \cdot \frac{1}{2\rho} + P_1 \tag{2.19}$$

2.5 Kinetic Decomposition and Combustion Analysis of Secondary Injection

Secondary injection in the expansion section of a nozzle leads to a far more complicated analysis than traditional De Laval flow analysis outlined in section 2.1. Injecting hydrogen peroxide requires the following new parameters to be considered: (1) Momentum and heat exchange between the injected fluid and core flow, (2) droplet vaporization, (3) chemical reaction of the vaporized injected liquid with the core flow, and (4) associated changes to chemical properties such as specific heat, c_p, and molecular weight, *W*. Shapiro [17] analyzes this problem qualitatively by introducing the concept of "Influence Coefficients" that can be used to solve for state variables using a spatial stepping analysis.

The influence coefficients are summarized in Fig. 2.2. In the top row, the independent variables are multiplied by their respective influence coefficient and added together as demonstrated in the equation below the table. They are called influence coefficients since they indicate the influence of each independent variable on each of the

	$\frac{dA}{A}$	$\frac{dQ - dW_x + dH}{c_pT}$	$4f\frac{dx}{D} + \frac{dX}{\frac{1}{2}kpAM^2} - 2y\frac{dw}{w}$	$\frac{dw}{w}$	$\frac{dW}{W}$	$\frac{dk}{k}$
$\frac{dM^2}{M^2}$	$-\frac{2\left(1+\frac{k-1}{2}M^2\right)}{1-M^2}$	$\frac{1+kM^2}{1-M^2}$	$\frac{kM^2\left(1+\frac{k-1}{2}M^2\right)}{1-M^2}$	$\frac{2(1+kM^2)\left(1+\frac{k-1}{2}M^2\right)}{1-M^2}$	$-\frac{1+kM^2}{1-M^2}$	-1
$\frac{dV}{V}$	$-\frac{1}{1-M^2}$	$\frac{1}{1-M^2}$	$\frac{kM^2}{2(1-M^2)}$	$\frac{1+kM^2}{1-M^2}$	$-\frac{1}{1-M^2}$	0
$\frac{dc}{c}$	$\frac{\frac{k-1}{2}M^2}{1-M^2}$	$\frac{1-kM^2}{2(1-M^2)}$	$-\frac{k(k-1)M^4}{4(1-M^2)}$	$-\frac{\frac{k-1}{2}M^2(1+kM^2)}{1-M^2}$	$\frac{kM^2-1}{2(1-M^2)}$	$\frac{1}{2}$
$\frac{dT}{T}$	$\frac{(k-1)M^2}{1-M^2}$	$\frac{1-kM^2}{1-M^2}$	$-\frac{k(k-1)M^4}{2(1-M^2)}$	$-\frac{(k-1)M^2(1+kM^2)}{1-M^2}$	$\frac{(k-1)M^2}{1-M^2}$	0
$\frac{d\rho}{\rho}$	$\frac{M^2}{1-M^2}$	$-\frac{1}{1-M^2}$	$-\frac{kM^2}{2(1-M^2)}$	$-\frac{(k+1)M^2}{1-M^2}$	$\frac{1}{1-M^2}$	0
$\frac{dp}{p}$	$\frac{kM^2}{1-M^2}$	$-\frac{kM^2}{1-M^2}$	$-\frac{kM^2[1+(k-1)M^2]}{2(1-M^2)}$	$-\frac{2kM^2\left(1+\frac{k-1}{2}M^2\right)}{1-M^2}$	$\frac{kM^2}{1-M^2}$	0
$\frac{dF}{F}$	$\frac{1}{1+kM^2}$	0	$-\frac{kM^2}{2(1+kM^2)}$	0	0	0
$\frac{ds/c_p}{\text{(Note 2)}}$	0	1	$\frac{(k-1)M^2}{2}$	$(k-1)M^2$	0	0

NOTES: (1) Each influence coefficient represents the partial derivative of the variable in the left-hand column with respect to the variable in the top row; for example

$$\frac{dM^2}{M^2} = -\frac{2\left(1+\frac{k-1}{2}M^2\right)}{1-M^2}\frac{dA}{A} + \frac{1+kM^2}{1-M^2}\frac{dQ-dW_x+dH}{c_pT} + \cdots - \frac{dk}{k}$$

Fig. 2.2 Influence coefficients for variable specific heat and molecular weight. Taken from Shapiro [17].

dependent variables (the variables on the left side). The formulation is such that the influence coefficients are only a function of Mach number and specific heat ratio (k in the table, γ in this paper). The independent variables are made of various components, and ones not previously defined are as follows: dQ is heat transferred from liquid droplets to core gas flow (negative in this case), dW_x is the work output, which is zero. The dH enthalpy term is defined by

$$dH = dh_{pr} - \left[h_L - h_V + \frac{v_g^2 - v_d^2}{2}\right]\frac{dw_L}{w} \tag{2.20}$$

where dh_{pr} is the constant pressure heat of combustion (assumed to be positive for exothermic reactions), h_L is the enthalpy of evaporated liquid at the liquid temperature, h_V is the enthalpy of the evaporated liquid at the core gas temperature, v_g and v_d are the core gas and droplet velocities, respectively, dw_L is the incoming mass flow rate of vaporized liquid, and w is the incoming core mass flow rate. Where only dw is specified, it is equal to dw_L in the case of this analysis.

In the momentum variable, the $4f\frac{dx}{D}$ represents losses due to friction and is neglected. The term dX is the drag force exerted on the core gas flow by the liquid droplets and k is the thermal conductivity of the gas. In the third part of the momentum variable, $y = \frac{v_d'}{v_g}$ is a velocity ratio, where v_d' is the forward velocity of the liquid. W is the apparent molecular weight of the gas.

The column on the left represents the dependent variables and represent, in order, the square of Mach number, velocity, speed of sound, temperature, density, pressure, thrust, and entropy. Note that the entropy term in only valid for non-reacting flow.

The control volume for this problem is depicted in Fig. 2.3. The core flow enters the control volume from the left-hand boundary of the image. The injected liquid droplets are assumed to lie outside of the control volume. Liquid droplets partially vaporize based on *dQ*, heat transfer from gaseous core flow to liquid droplets, and enter the control volume as dw_L, vaporized and at same temperature and velocity as the liquid, but same pressure as the core gas flow. The liquid droplets exert a drag force on the core flow and accelerate accordingly. Since the liquid droplets are at a significantly different velocity from the core flow, their time step is altered accordingly.

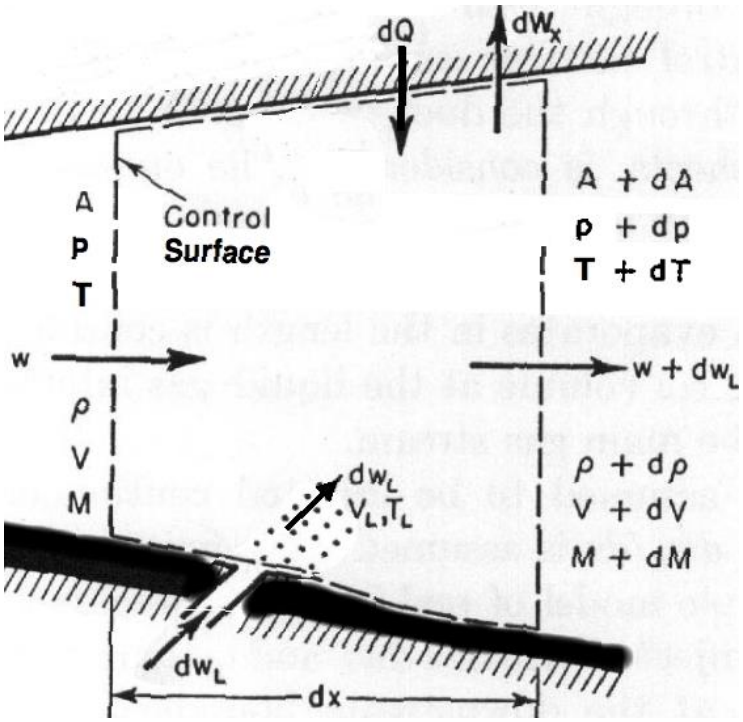

Fig. 2.3 Control volumes for secondary injection.

The hydrogen peroxide is assumed to be inert until it has been converted to a gaseous phase. At this point it is assumed to react with the core according to the implemented kinetic model, which will be detailed later.

2.5.1 *Droplet Evaporation Model*

Droplets are assumed to be spherical and evenly dispersed through the continuous core flow. Momentum exchange is assumed to occur only due to drag, and only convective heat transfer is considered. The model formulation used will be a non-equilibrium Langmuir-Knudsen evaporation model as outlined by Miller [18]. The following equations describe the liquid, 90% hydrogen peroxide droplet velocity (v_d), droplet temperature (T_d), and droplet mass (m_d):

$$\frac{dv_d}{dt} = \frac{X}{m_d} = \left(\frac{f_1}{\tau_d}\right)\left(v_g - v_d\right) \tag{2.21}$$

$$\frac{dT_d}{dt} = \frac{Q_d + \dot{m}_d h_{fg}}{m_d c_{p,liq}} = \frac{f_2 Nu}{3Pr\ \tau_d}\frac{c_{p,g}}{c_{p,liq}}\left(T_g - T_d\right) + \left(\frac{h_{fg}}{c_{p,liq}}\right)\frac{\dot{m}_d}{m_d} \tag{2.22}$$

$$\frac{dm_d}{dt} = -\frac{Sh}{3Sc_g}\left(\frac{m_d}{\tau_d}\right)\ln\left(1 + B_{M,neq}\right) \tag{2.23}$$

The time term, $\tau_d = \rho_d D^2/(18\mu_g)$ is the particle time constant for Stokes flow, where *D* is the droplet diameter and μ_g is the dynamic viscosity of the core flow. The f_1 and f_2 terms are dimensionless variables, where the first is a drag coefficient correction to Stokes flow ($C_D = f_1\ 24/Re$) and the second is correction to the heat transfer coefficient due to the blowing effect of droplet evaporation ($q'' = f_2 h\Delta T$). The drag coefficient is defined using a correlation suggested by Ren [19].

$$C_D = \frac{24}{Re}(1 + 0.15Re^{0.687}) + \frac{0.42}{1 + 4.24 \times 10^4 Re^{-1.16}} \tag{2.24}$$

This correlation was determined by Clift and Gauvin [20] and is recommended for Reynolds number bellow 3×10^5. The heat transfer correction is determined using the non-dimensional evaporation parameter (β).

$$f_2 = \frac{\beta}{e^{\beta} - 1} \tag{2.25}$$

$$\beta = -\left(\frac{3}{2} Pr \cdot \tau_d\right) \frac{w_d}{m_d} \tag{2.26}$$

In Eq. (2.21) X is the drag force exerted on the liquid droplet and Q_d is the heat transfer imparted to the droplet. Note that the heat transfer rate heats up the liquid and drives the phase change. Evaporated liquid entering the control volume is assumed to be gas at the same temperature as the liquid.

All standard non-dimensional parameters are defined as follows:

Reynolds Number $$Re = \frac{\rho_g (v_g - v_d) D}{\mu_g} \tag{2.27}$$

Prandtl Number $$Pr = \frac{\mu_g c_{p,g}}{k_g} \tag{2.28}$$

Schmidt Number $$Sc = \frac{\mu_g}{\rho_g D_{AB}} \tag{2.29}$$

Nusselt Number $$Nu = 2 + 0.552 Re^{\frac{1}{2}} Pr^{\frac{1}{3}} \tag{2.30}$$

Sherwood Number $$Sh = 2 + 0.552 Re^{\frac{1}{2}} Sc^{\frac{1}{3}} \tag{2.31}$$

The Nusselt Number and Sherwood Number both use Ranz and Marshall's [21] empirical correlations for external convection around a sphere. The parameter D_{AB} is the binary diffusivity of hydrogen peroxide into the core gas. It was calculated using methods outlined in chapter 11 of *The Properties of Gases and Liquids* [22].

The enthalpy of vaporization (h_{fg}) is calculated to correlate with the actual liquid temperature as follows:

$$h_{fg} = h_{fg,T_B}\left(\frac{T_C - T_d}{T_C - T_B}\right)^{0.38} \tag{2.32}$$

where h_{fg,T_B} is the enthalpy of vaporization at the atmospheric boiling point, T_B is the atmospheric boiling point, and T_C is the critical temperature of the liquid.

The specific driving potential in Eq. (2.23) is formulated as to allow for non-equilibrium heat and mass transfer. Miller [18] found use of the non-equilibrium Langmuir-Knudsen evaporation be particularly important for very small droplets (i.e. < 50 μm) and high heat transfer rates, both of which are imbedded in this problem. $B_{M,neq}$ is the non-equilibrium Spalding transfer number for mass and is defined as

$$B_{M,neq} = \frac{Y_{s,neq} - Y_G}{1 - Y_{s,neq}} \tag{2.33}$$

where Y_G is the far-field vapor mass fraction and $Y_{s,neq}$ is the non-equilibrium vapor surface mass fraction. The surface mass fraction is determined from the surface molar fraction as follows:

$$Y_{s,neq} = \frac{\mathcal{X}_{s,neq}}{\mathcal{X}_{s,neq} + \left(1 - \mathcal{X}_{s,neq}\right)\frac{\mathrm{W}}{\mathrm{W_v}}} \tag{2.34}$$

where $\mathcal{X}_{s,neq}$ is the non-equilibrium surface molar fraction,

$$\mathcal{X}_{s,neq} = \frac{P_{atm}}{P}\exp\left[\frac{h_{fg}}{R_g}\left(\frac{1}{T_B} - \frac{1}{T_d}\right)\right] - \left(\frac{\mathrm{L_K}}{\mathrm{D}/2}\right)\beta \tag{2.35}$$

and L_K is the Knudsen layer thickness.

$$L_K = \frac{\mu_g\sqrt{2\pi T_d R_g}}{S_c P} \tag{2.36}$$

The first term in Eq. (2.35) is the saturation pressure ratio as determined using the Clausius-Clapeyron equation for constant latent heat. The second term is the non-

equilibrium term which allows the droplets to become superheated. As stated before, this is a common phenomenon in supersonic combustors. The relationship between the droplet evaporation rate and the surface molar fraction is very non-linear. In practice, it was found that using a bisection root finding method to determine the correct evaporation rate yielded the best results.

2.5.2 *Distribution of Dispersed Droplets*

Droplets are initially traveling at a much slower velocity than the core gas flow. The droplet dispersion "stretches" as the velocity increases, as illustrated in the Fig. 2.4.

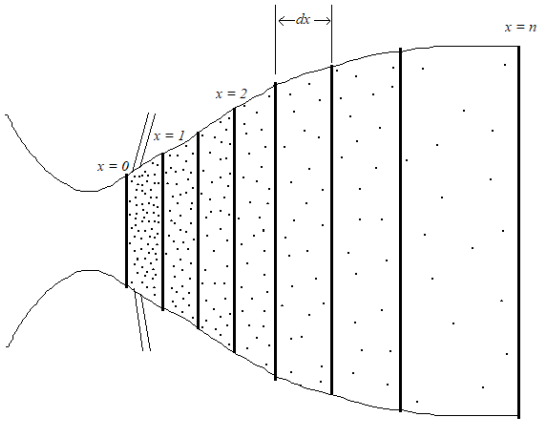

Fig. 2.4 Droplet distribution as liquid phase accelerates.

While the droplet flow rate, $\dot{n}_d$, remains constant since the flow is assumed to be at steady state conditions, the droplet velocity increases due to the drag force the core flow exerts on the droplets. At each step, the total number of droplets inside the control volume must be determined.

$$n_d = \dot{n}_d \Delta t_d \tag{2.37}$$

where

$$\Delta t_d = \frac{dx}{v_d} \tag{2.38}$$

The flow rate of the added vapor, dw, heat transfer, dQ, and drag force exerted on the core gas, dX, then become

$$dw = -w_d \cdot n_d \tag{2.39}$$

$$dQ = -\frac{Q_d \cdot n_d}{w} \tag{2.40}$$

$$dX = X \cdot n_d \tag{2.41}$$

2.5.3 Kinetic Hydrogen Peroxide Decomposition

The decomposition on hydrogen peroxide is assumed to be a first-order reaction with the reaction rate governed by the reaction rate coefficient as follows:

$$\dot{M}_{hp} = -K \cdot M_{hp} \tag{2.42}$$

where M_{hp} is the molarity of hydrogen peroxide, in units of $\mathrm{mols/m^3}$ and K is the reaction rate coefficient with units of $\mathrm{sec^{-1}}$. The reaction rate coefficient is found using the Arrhenius equation.

$$K = A_0 \exp\left(\frac{-E_a}{R_u T_g}\right) \tag{2.43}$$

Here A_0 is the frequency factor or pre-exponential factor and E_a is the activation energy. Corpening [23] suggests values of $A_0 = 10^3/\mathrm{s}$ and $E_a = 200{,}864.6\ \mathrm{J/mol}$. These are rate constants for thermal decomposition of hydrogen peroxide. Presumably the hot hydrocarbons of the primary flow would have a catalyzing effect, so using these would be a slightly conservative approach.

The rate change of molarity is wanted in terms of mass flow rate.

$$dM_{hp} = -K \cdot M_{hp} dt = -K \cdot M_{hp} \frac{dx}{v_g} \tag{2.44}$$

$$M_{hp} = \frac{\dot{N}_r}{\dot{V}} = \frac{\frac{w_r}{W_{hp}}}{\frac{w}{\rho_g}} = \frac{w_{hp}}{w}\frac{\rho_g}{W_{hp}} \tag{2.45}$$

Here $\dot{N}_r$ is the molar decomposition rate, $\dot{V}$ is the core gas volume flow rate, and w_r is the hydrogen peroxide mass decomposition rate.

$$\frac{dM_{hp}}{M_{hp}} = \frac{dw_r}{w_{hp}} - \frac{dw}{w} + \frac{d\rho_g}{\rho_g} = -K \cdot \frac{dx}{v_g} \tag{2.46}$$

This can be transformed to the same style as the influence coefficients in Ref. [17] by substituting in the tabulated value for $\frac{d\rho_g}{\rho_g}$.

$$\frac{dw_r}{w_{hp}} = -\frac{M^2}{w_{hp}}\frac{dA}{A} + \frac{1}{1-M^2}\frac{dQ+dH}{c_{p,g}T_g} + \frac{\gamma M^2}{2(1-M^2)}\left(\frac{dX}{\frac{1}{2}\gamma PAM^2} - 2y\frac{dw}{w}\right)$$
$$+\frac{1-\gamma M^2}{1-M^2}\frac{dw}{w} - \frac{1}{1-M^2}\frac{dW}{W} - K\frac{dx}{v} \tag{2.47}$$

The enthalpy of combustion is calculated using CEA. At each step, the products of the previous step are input as fuel and the reacted hydrogen peroxide calculated in Eq. (2.47) is input as the oxidizer. For simplicity, evaporated 90% hydrogen peroxide is assumed to stay in the same mixture ratio as a vapor. Hydrogen peroxide and water vapor are input into CEA in that mixture ratio, and unreacted peroxide remains in that mixture ratio. Unreacted water vapor is counted with hydrogen peroxide vapor, and reacted water is counted with combustion products. The enthalpy of combustion is calculated by taking the change in enthalpy of formation from the reactants to the products. The M = 0 condition is used and other properties such as molecular weight and specific heat can be taken from there as well. Using this method, the completeness of decomposition of the injected peroxide can be determined. It will be shown hereafter how test data correlates

with the results of this simulation can be used to determine an optimal design configuration.

The algorithm used in the kinetic decomposition / combustion model is summarized in Fig. 2.5.

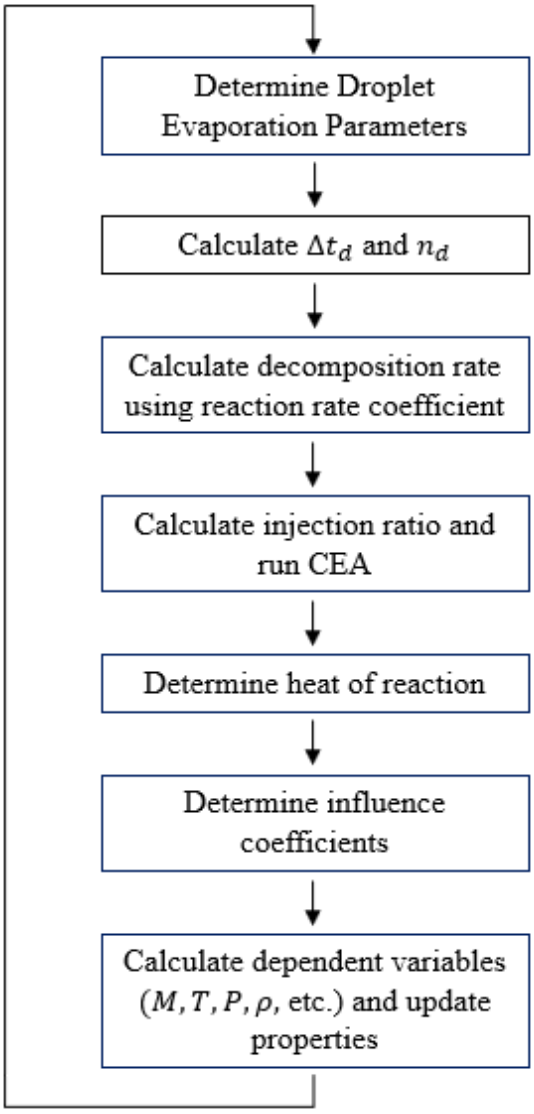

Fig. 2.5 Decomposition model algorithm.

Using this method, the completeness of decomposition of the injected peroxide can be determined. It will be shown hereafter how test data correlates with the results of this simulation can be used to determine an optimal design configuration.

CHAPTER 3

EXPERIMENTAL SETUP

3.1 TAN Nozzle Modifications

The legacy system used by Ref. [11] was used as the thrust chamber, with the original nozzle throat modified to match the GOX/ABS TAN system used in Ref. [9]. Baseline tests were performed using a 2.594:1 expansion ratio conical nozzle. This nozzle was optimized for ambient conditions in Logan, UT. In all tests using secondary injection, this low expansion ratio nozzle, made from machined graphite, was replaced by the TAN nozzle. Figure 3.1 shows the TAN nozzle design. The nozzle was built in modular fashion, allowing the injector section to be swapped out in order to study the effects of secondary injection position and angle. The nozzle contour was designed using the method of characteristics as described in chapter 11 of Anderson [24]. A maximum angle of 26.126° was used. This was a conservative maximum turning angle used to ensure that

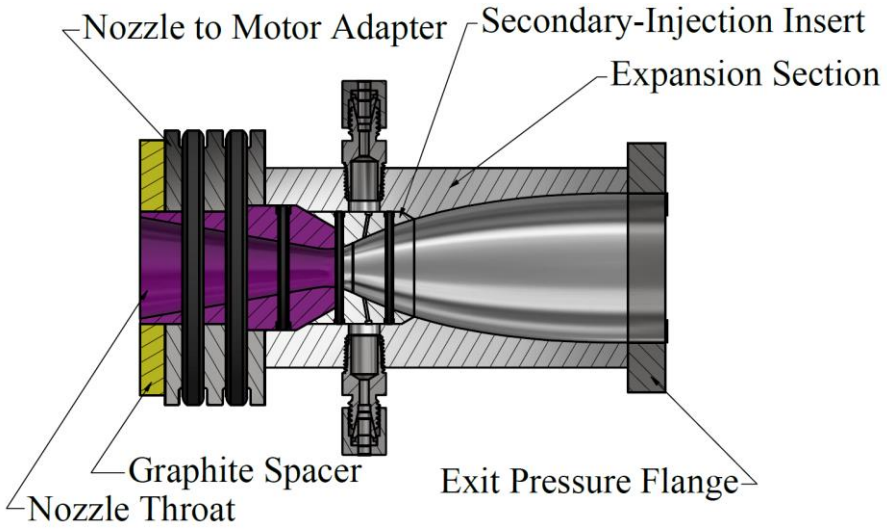

Fig. 3.1 TAN nozzle with secondary H_2O_2 injection.

there were no losses due to too short of a turning section, and to allow for a somewhat longer nozzle for better mixing with secondary injection.

Figure 3.2 shows the secondary injection configurations that were considered for this test campaign. For the initial configuration, the 10° forward-facing injection angle was selected. This is drastically different from the injector angle used in first TAN test campaign in Ref. [34], which had a backward facing injector, or injecting with the flow. Since hydrogen peroxide has an activation energy that must be met before it will decompose, it was decided that it would need increased dwell time and penetration into the core flow combustion products in order to achieve adequate mixing and dwell time.

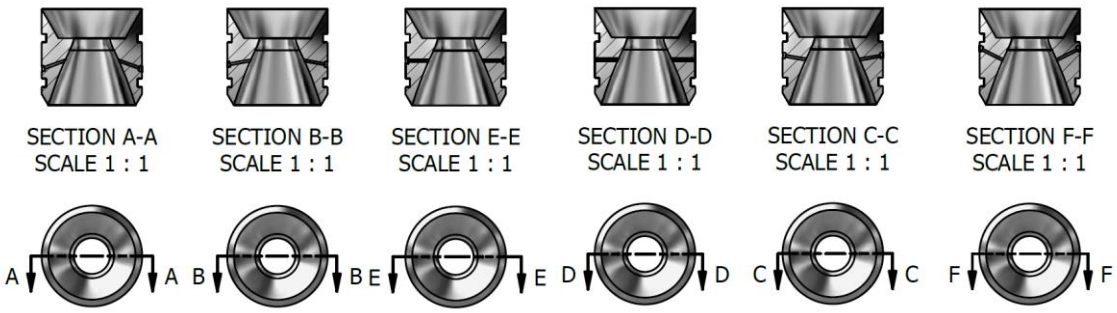

Fig. 3.2 H_2O_2 secondary injection inserts considered for this study.

The injector location was chosen using a conservative approach. Flow separation is predicted to occur after the wall pressure drops below ambient conditions, about 12.4 psi. Various chamber pressures were considered for the test campaign, and as an estimate for where the wall pressure would drop below ambient, the plot in Fig. 3.3 was generated. The lowest predicted chamber pressure was 150 psi, so the axial location that corresponded with where the wall pressure was equal to the ambient pressure for 150 psi

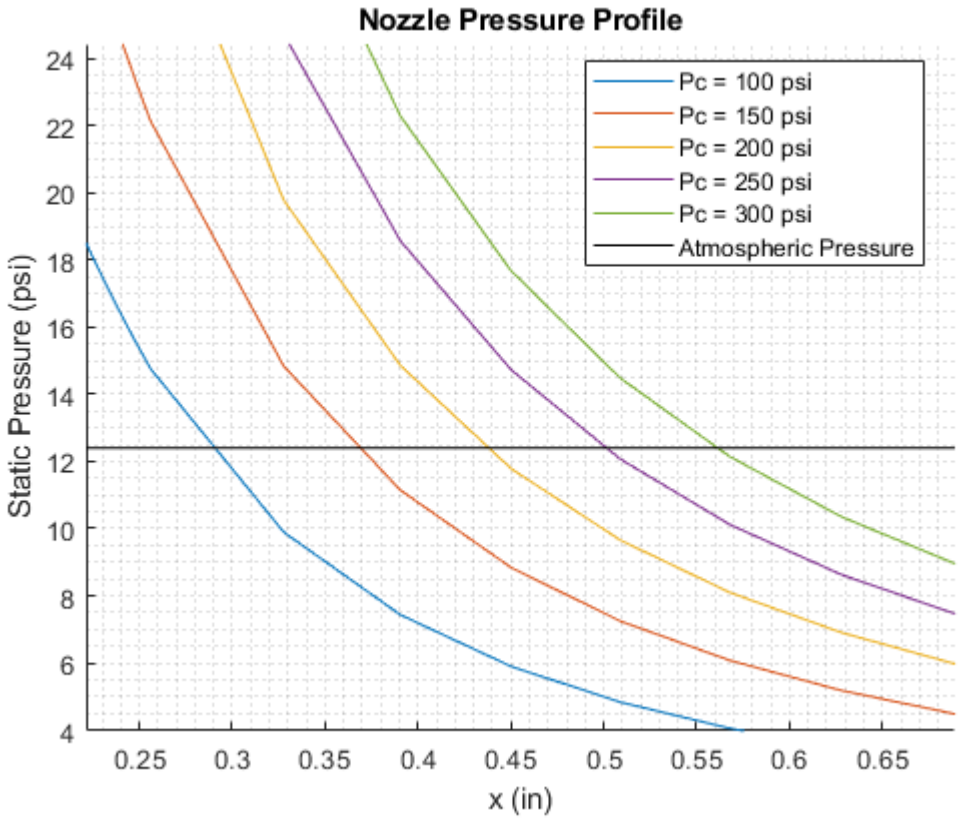

Fig. 3.3 Nozzle wall pressure prediction using method of characteristics at various chamber pressures.

was chosen. This corresponded to about 0.37 inches downstream of the throat.

The injector configuration has a large effect on the performance of the TAN system. The location, diameter, and orientation all greatly affect penetration, mixing, and atomization, which all have a great impact on nozzle performance. The location and orientation of the injector were selected such that they would give optimal mixing and dwell time. This injector diameter was chosen to be 0.026 inches. This was a reasonable small diameter that was still machinable. A smaller diameter would be preferable for better penetration and mixing.

The nozzle expansion ratio was chosen to be 16:1. At the combustion operating

chamber pressures, a shock wave [24] was predicted to develop upstream of the nozzle exit with no secondary injection. This nozzle is optimized for near vacuum applications. The idea is that secondary injection will increase the pressure inside the nozzle, and will push any incipient shockwave further downstream and optimally out of the nozzle. Materials in the flow path of combustion products were chosen that had highly heat resistant properties. The nozzle throat was made of graphite and the injector insert and nozzle expansion sections were made of Inconel, a nickel-chromium based superalloy with excellent heat and corrosion resistance.

3.2 Ignition System

The base of the ignition system is the USU patented arc-ignition technology for hybrid rocket systems [12]. This ignitor operates from the electrical breakdown properties of certain 3-D printed thermoplastics such as ABS and High-Impact-Polystyrene. Two electrodes are imbedded in the top of a shelf in the ignitor cap. This section acts as a small pre-combustion chamber. This shelf is positioned such that the injected GOX impinges and recirculates before continuing into the fuel port. The electrode ends are typically about ¼ inch apart. See Fig. 3.4a.

When an electrostatic potential is placed across the electrodes, electricity flows through a pre-existing arc-track, pyrolyzing fuel in its path (see Fig. 3.4b). This pyrolyzed fuel reacts immediately with GOX flow and initiates combustion. The arc-ignition process is extremely energy efficient, requiring as little as 10 W for less than one second. Typical ignition energies are less than 10 Joules.

As stated in section 1.6, GOX/ABS combustion generates temperatures exceeding 2800°C. Once combustion has been initiated using GOX, 90% hydrogen peroxide is

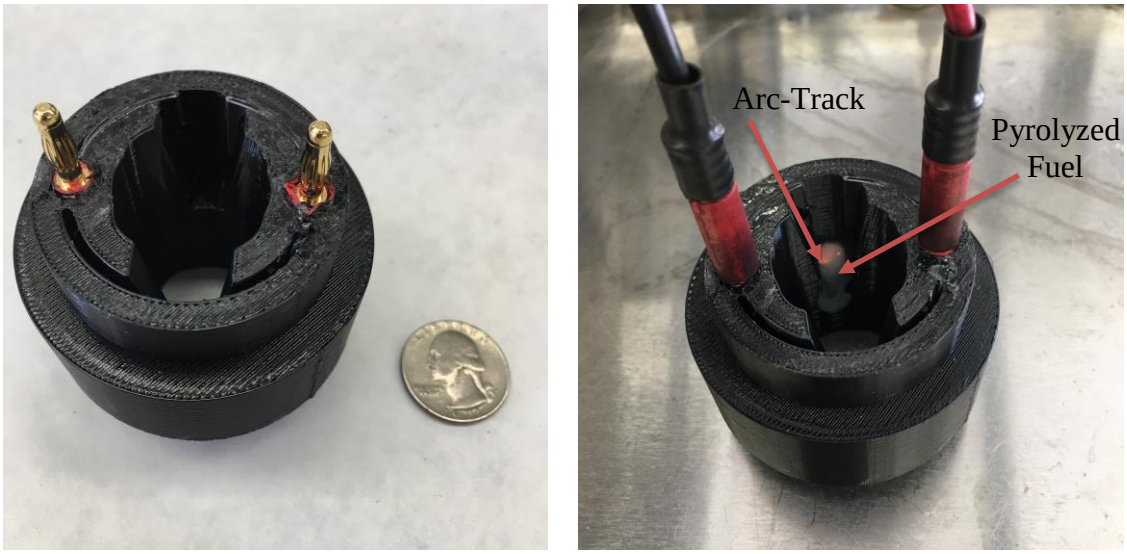

a) Relative size of igniter cap. *b) Arc-track and pyrolyzed fuel.*

Fig. 3.4 Arc-ignitor cap used in hydrogen peroxide injected TAN system.

injected into the hot combustion products. With proper atomization, there exists sufficient energy in the combustion chamber to decompose the hydrogen peroxide. The injector setup is shown later in Fig. 3.12. GOX is injected through the outer concentric injection ports, and hydrogen peroxide through the middle hollow-cone style injector. Once full decomposition has been initiated, the reaction is self-sustaining and the GOX is shut off. Overall for typical tests, the arc-ignitor is activated for two seconds and GOX is used for two seconds, one second before peroxide injection and one second after. See Fig. 3.14 later in the chapter for full example firing sequence.

3.3 High Test Peroxide Solution Preparation

High concentration hydrogen peroxide (solutions of greater than 70% concentration), are typically referred to in industry as high-test peroxide, or HTP. Commercial vendors for HTP typically require a large minimum order and have strict

compliance rules for storage. USU does not have the existing infrastructure to store large quantities of HTP. As a means of minimizing risk and obtaining the needed HTP, the USU Propulsion Research Lab has developed a condensation procedure to safely manufacture small quantities of HTP from readily available 30% hydrogen peroxide [25]. Fig. 3.5 shows the evaporator arrangement with the laboratory-quality Wilmad WG-EV311 rotary evaporator installed under a fume hood to collect any extraneous peroxide vapor.

Fig. 3.5 Rotary evaporator system used to condense HTP from 30%.

The concentration procedure is derived from the work of Rarata and Surmacz (Poland Aviation Institute, [26]). The 30% peroxide is put into the distillation flask, which is place in a 55° water bath while rotating. The system is put under vacuum to the boiling point of the peroxide solution. Since water has a lower boiling point than peroxide, water evaporates faster than peroxide evaporates. In this way the temperature is kept low enough to retard background peroxide decomposition. Vapor is drawn across cooling coils chilled by ice-water, and condenses into the condensation flask. As the peroxide concentration in the distillation flask rises, the boiling point drops, so the

vacuum is gradually increased throughout the operation. Using this procedure about 100 g of 90% hydrogen peroxide is concentrated from the original 500 mL of 30% peroxide, and typically takes one to one and a half hours.

As an operating principle, no more than one day of testing's worth of HTP is kept on hand. Any unused portion is diluted down to 50%.

3.4 Test Apparatus

Figure 3.6 presents the Piping and Instrumentation Drawing (P&ID) of the TAN test system. For the TAN performance tests, a secondary peroxide tank along with associated piping were added to the original system. Priming valves, shown in Fig. 3.6 as PAS #3 and SV #6 were added to provide a less noisy mass flow rate measurement. These valves allowed the lines to be primed, removing air in the lines and especially in the flow venturis. After discovering the systems response to cold weather conditions inherent with testing in winter conditions in Logan, UT, heaters were added to multiple locations in the peroxide flow path. All lines are stainless steel, and were passivated using citric acid [27].

Measurements available include motor thrust, primary and secondary peroxide mass flow rate, pre-lead GOX mass flow rate, primary and secondary injection pressures, chamber pressure, exit pressure, total consumed propellant mass, peroxide tank temperatures, and main peroxide injection temperature. Multiple thermocouple measurements were also installed as a part of the fire control safety management system.

Figure 3.7 through Fig. 3.10 show the actual test set up. Less visible in the figures are the three tanks, control box, dump valves, and dump bucket on the bottom shelf of the cart. Both peroxide tanks are pressurized from the same nitrogen tank. The GOX tank is a

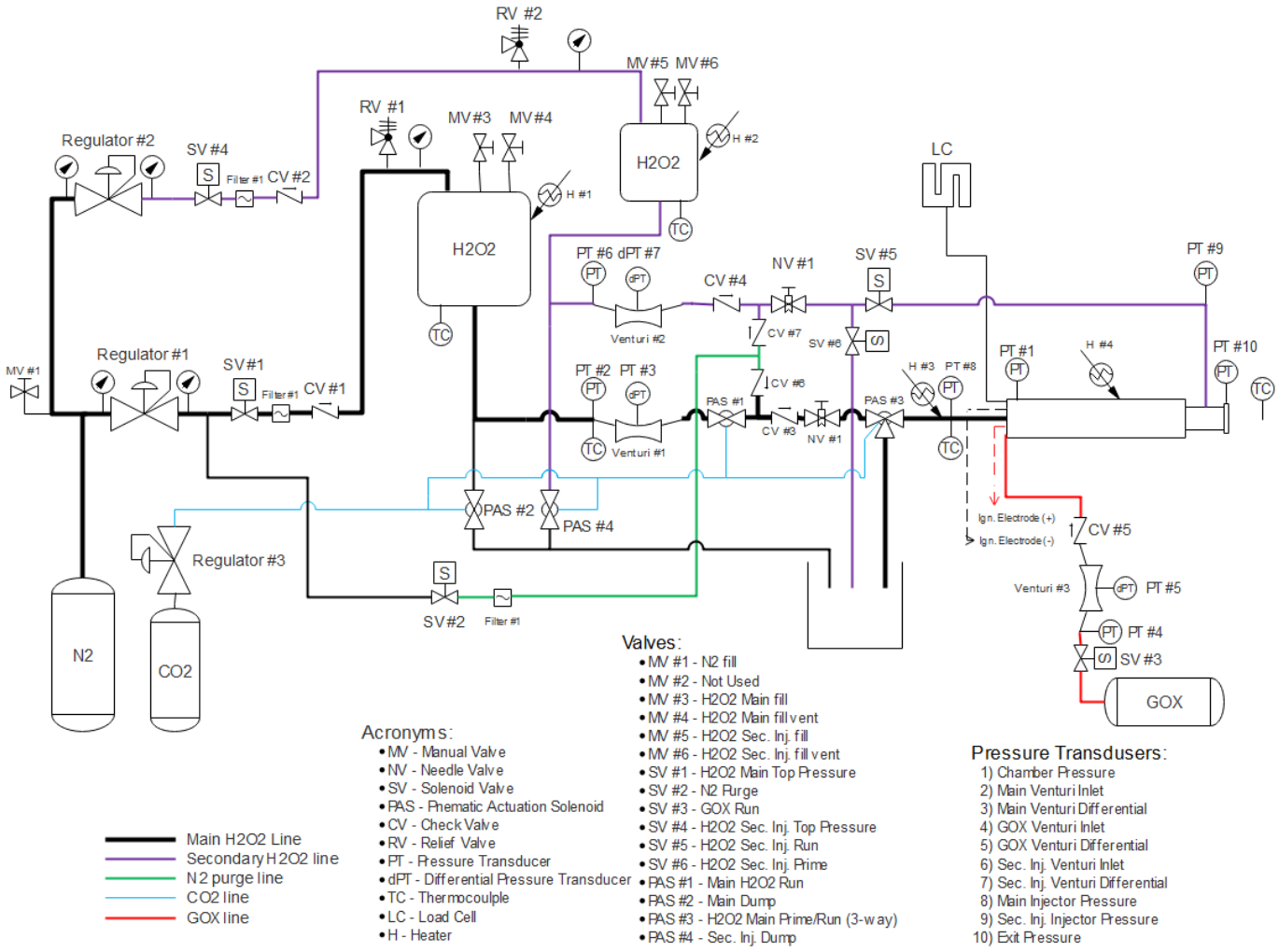

Fig. 3.6 Piping and instrumentation diagram of hydrogen peroxide injecting thrust augmenting nozzle test setup.

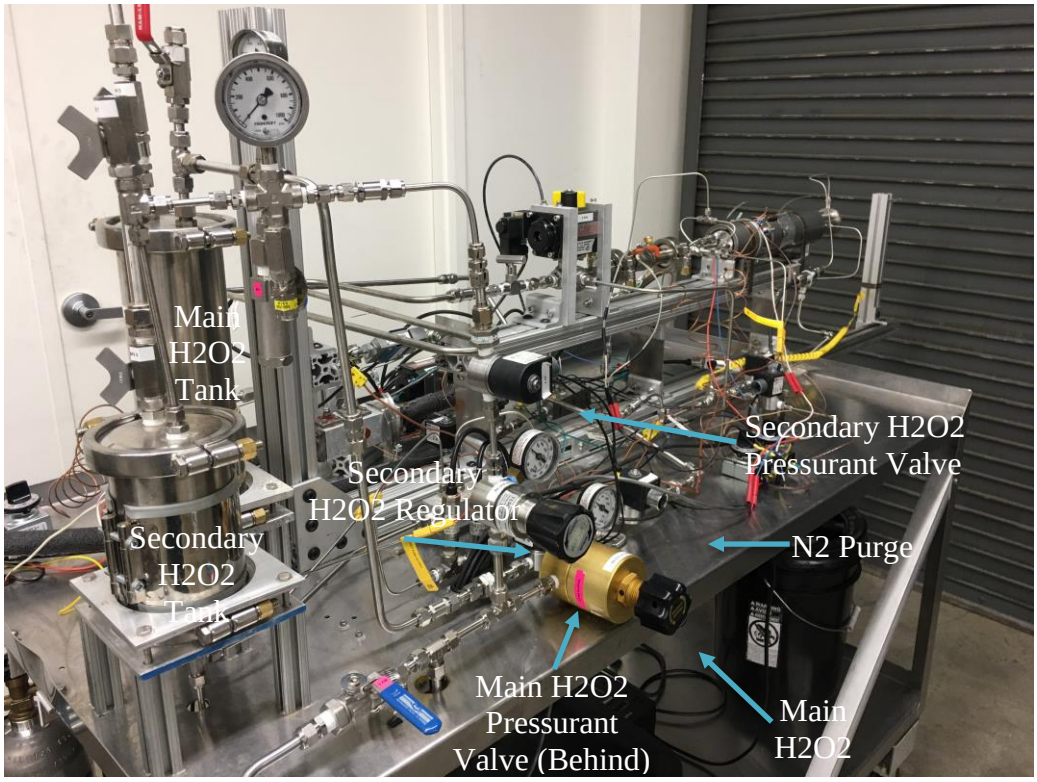

Fig. 3.7 Hydrogen peroxide injecting TAN test setup view 1.

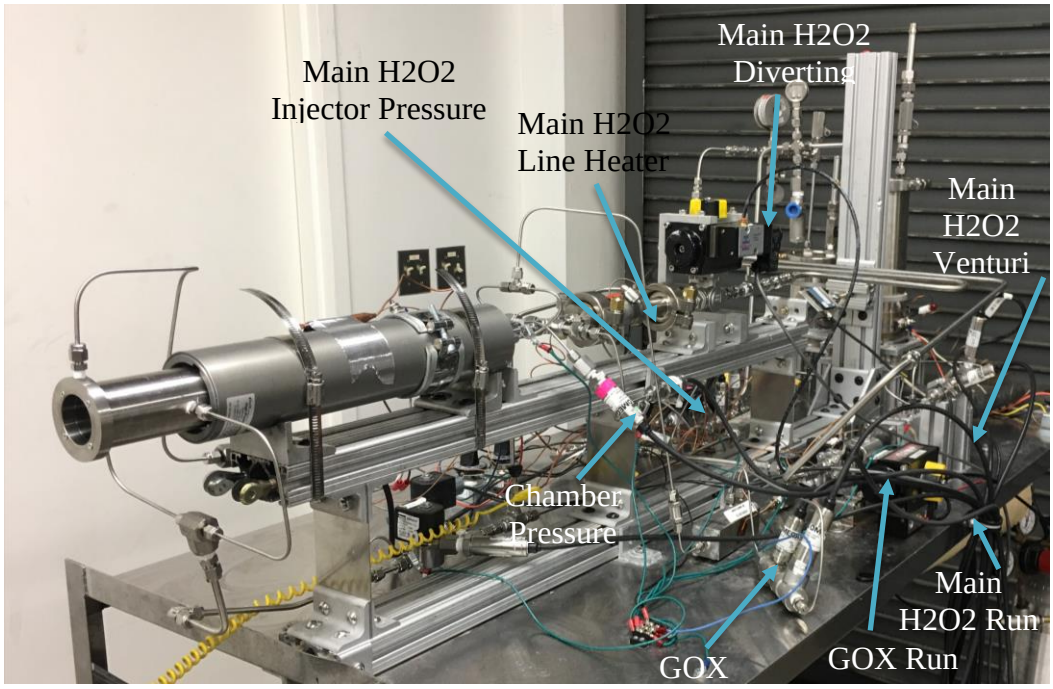

Fig. 3.8 Hydrogen peroxide injecting TAN test setup view 2.

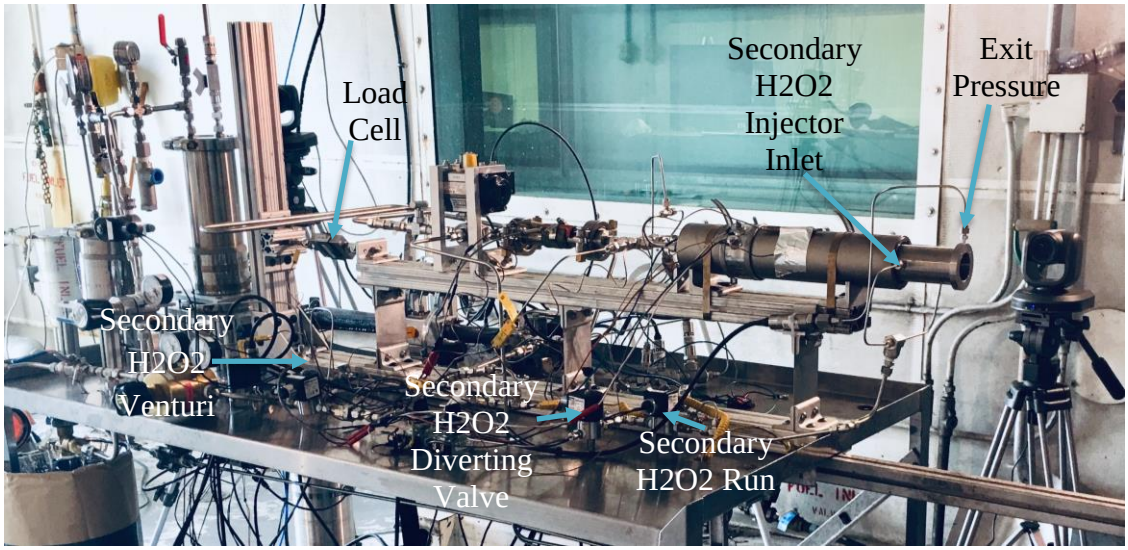

Fig. 3.9 Hydrogen peroxide injecting TAN test setup view 3.

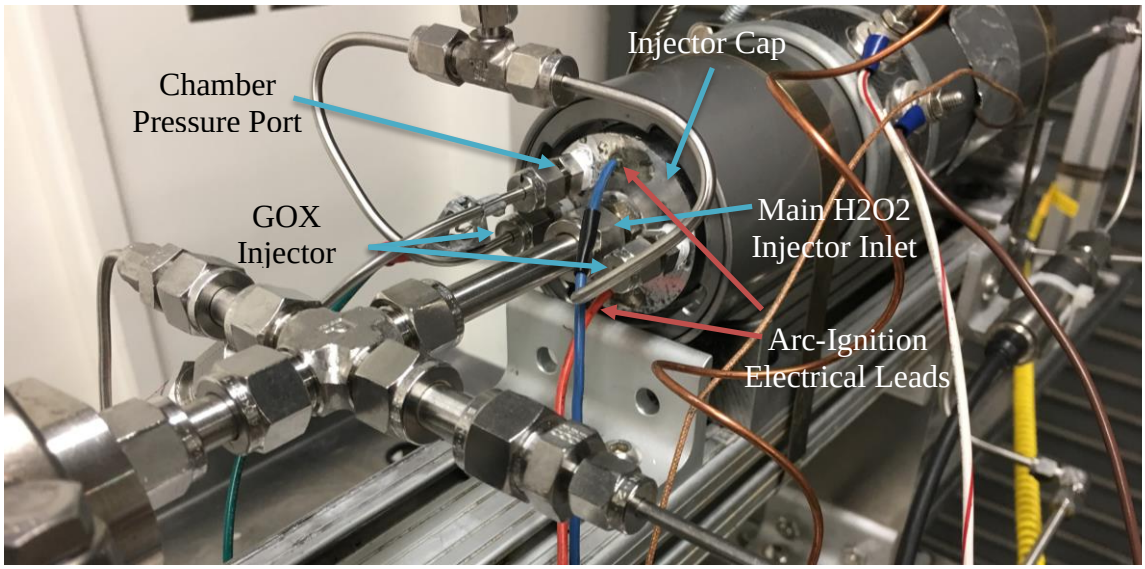

Fig. 3.10 Aft view of injector cap.

small carbon composite overwrap paintball tank. The CO2 tank provides pilot pressure for the four pneumatic actuated ball valves. The dump valves are used to remotely drain the peroxide tanks into the dump bucket, which is partially filled with water.

Figure 3.11 shows the hybrid rocket motor used in the test campaign. The three-

piece fuel grain consists of the 3D-printed arc-ignition cap, extruded fuel grain, and 3D-printed helical fuel grain insert. Making the grain in this manner significantly reduces the manufacturing cost. Details of the injector cap can be seen in Fig. 3.10 through Fig. 3.12.

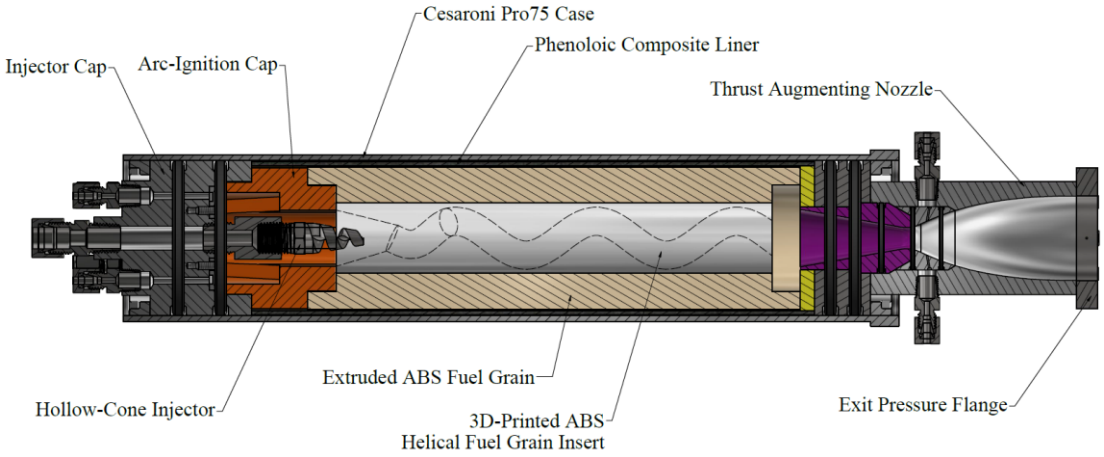

Fig. 3.11. Cut-away of hybrid rocket motor with TAN nozzle (colors added for better visibility).

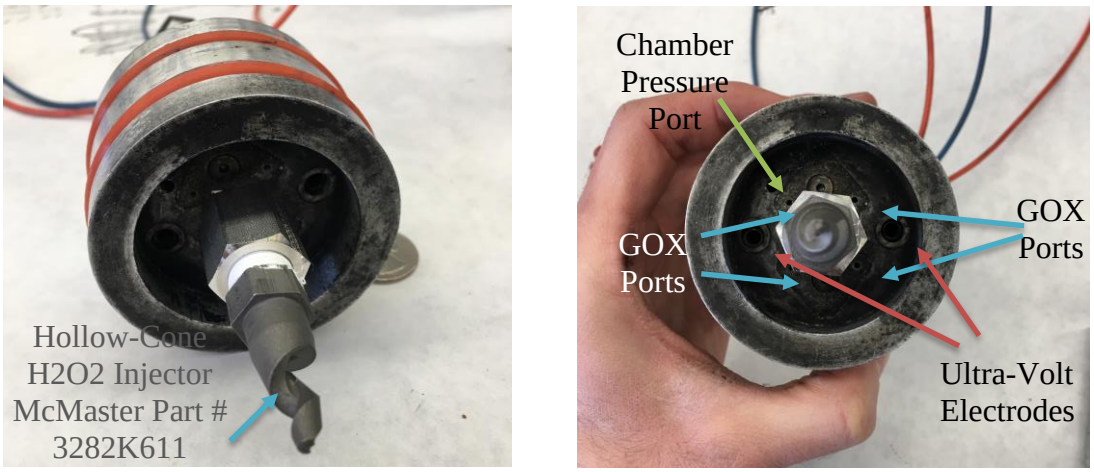

a) Injector cap. *b) Injector cap front view.*

Fig. 3.12. Coaxial duel-oxidizer injector cap.

The coaxial design helps increase burn uniformity. The hollow cone injector was installed following the guidance of Anthione et al. [28]. Various injector configurations

were tested by Ref. [11], finding the hollow-cone to supply shorter latencies and higher combustion efficiency.

In Fig. 3.13 and Fig. 3.14, the overall and valve operations are shown. Blue means activated and all other time are deactivated. All valves are normally closed. PAS 3 is normally in the mode of directing flow to the motor, and diverts flow to the dump bucket when activated. The firing sequence is led by both peroxide pressurant valves opening to ensure the tanks are brought up to full pressure before firing. The primary peroxide flow uses a one two-way valve and one three-way valve, so their timings overlap. The secondary peroxide flow uses two two-way valves, so their timings are staggered. The end of the firing sequence is followed by a purge sequence, which purges the peroxide lines with nitrogen through both diversion valves, and then pushes the last slug of peroxide through the motor/nozzle.

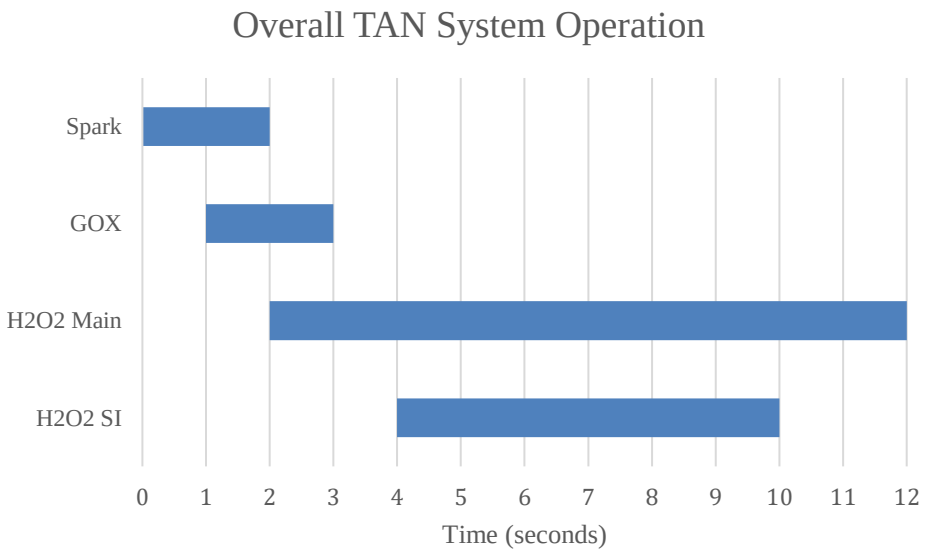

Fig. 3.13 Overall propellant operations of TAN system for typical burn.

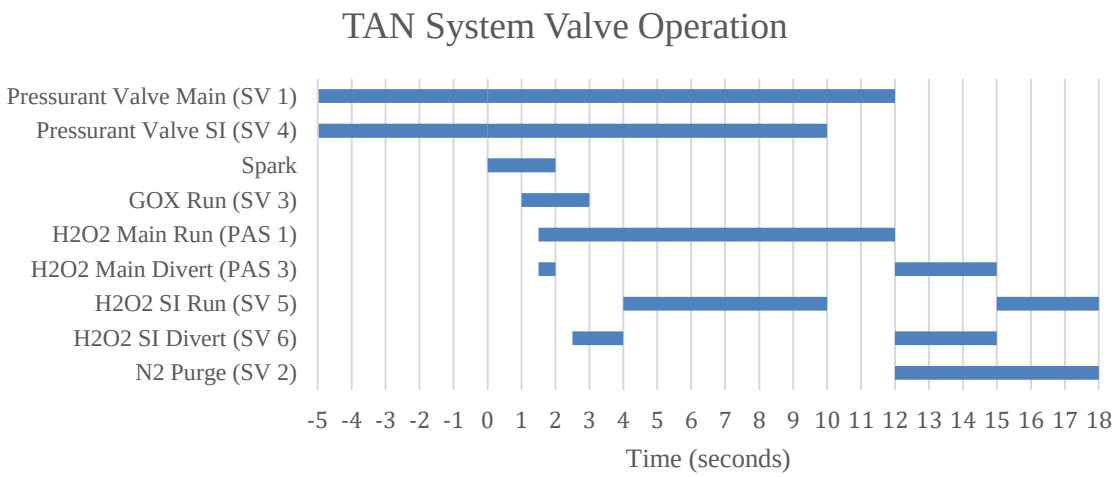

Fig. 3.14 Firing sequence for TAN system for typical burn.

CHAPTER 4

RESULTS AND DISCUSSION

The results of 14 successful tests will be presented. Of those tests, eleven used the TAN nozzle with secondary peroxide injection and three used the TAN nozzle without secondary injection. The tests using secondary peroxide injection will be referred to as TAN tests, and those that did not use secondary injection will be referred to as baseline tests. The first two TAN tests used a cylindrical fuel port. A helical fuel grain was used for the remainder of tests. While the parameters of the primary flow were kept as consistent as possible, the secondary mass flow rate was varied to characterize the augmentation response to varying augmentation ratio. Table 4.1 summarizes the test parameters.

Table 4.1 Test matrix summary

Date	Test Type	Fuel Grain	Burn Duration (s)	SI Duration (s)	Approx. SI Flow Rate (g/s)	Fuel Mass Consumed (g)
2/8/2019	Baseline	Helical	9	-	-	241
3/20/2019	Baseline	Helical	10	-	-	231
4/24/2019	Baseline	Helical	10	-	-	259
10/11/2018	TAN	Straight	7	4	16	71
10/17/2018	TAN	Straight	8	4	6.5	96
10/30/2018	TAN	Helical	12	8	12	269
11/9/2018	TAN	Helical	13	8	11.5	280
3/18/2019	TAN	Helical	10	6	10	268
3/25/2019	TAN	Helical	10	6	19	251
3/26/2019	TAN	Helical	10	6	24	247
3/30/2019	TAN	Helical	10	6	15	265
4/1/2019	TAN	Helical	10	6	5.5	259
4/24/2019	TAN	Helical	10	6	11	256

4.1 Thrust Augmentation using Cylindrical Port Fuel Grains

A cylindrical fuel grain was used to fine tune the test set up and was then used for the first TAN tests. Figure 4.1 shows the exhaust plume before and after commencement of secondary injection.

a) Fully Started Before TAN Injection *b) TAN Injection*

Fig. 4.1 Visual of TAN injection with cylindrical fuel port (10/17/2018).

As can be seen from Fig. 4.1, once the secondary injection begins, the plume shrinks. Though the phenomenon was not captured well by the cameras, the plume visually appeared darker once secondary injection began. Dark streaks in the plume were visible, giving it a “forked” look. This clearly indicated that the plume was being cooled and that little to no combustion of secondarily injected peroxide was happening.

Figure 4.2 shows the thrust curve of a TAN burn using a cylindrical port along with the secondary mass flow rate. The thrust curve shows no noticeable sign of an increase in thrust that correlates with the timing of the secondary injection. The cylindrical port configuration was used with two different secondary injection mass flow rates. With the higher mass flow rate of the first test, approximately 16 g/s of hydrogen peroxide, the cooling effect was even more pronounced. This lack of secondary injection

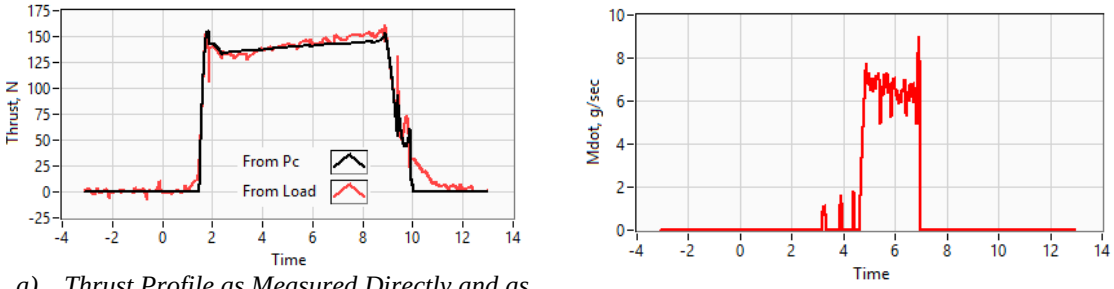

a) Thrust Profile as Measured Directly and as Calculated from Chamber Pressure.

b) Mass Flow Rate of Secondary Injected Peroxide

Fig. 4.2 Thrust and mass flow rate of TAN injection with cylindrical port (10/17/2018).

combustion likely resulted from how fuel lean the core flow was. Figure 4.3 shows a comparison of the flow rates of the oxidizer, fuel, and the total flow rate.

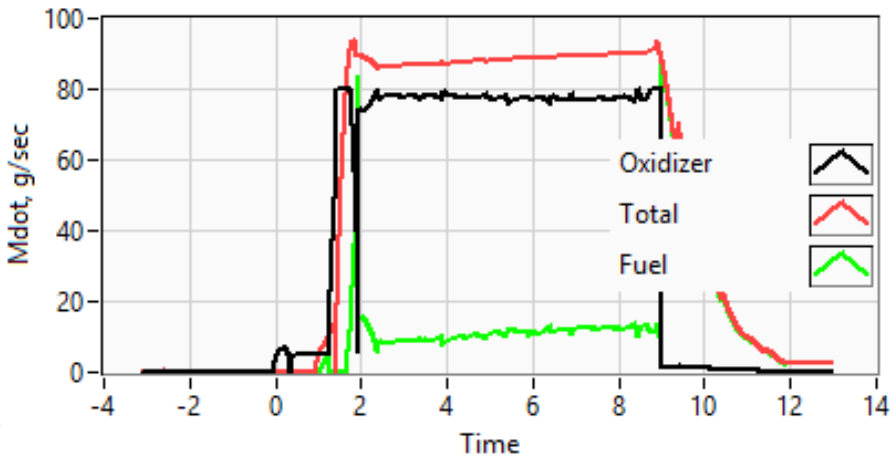

Fig. 4.3 Mass flow rate of core flow (10/17/2018).

The core flow was exceptionally fuel lean with an $O/F \approx 7.2$. This value is quite a bit larger than the stoichiometric O/F at approximately 5.5. It is possible that some thermal decomposition did occur in the nozzle since the adiabatic flame temperature at an O/F ratio of seven is quite hot, around 2600 K; however, since the adiabatic

decomposition temperature of 90% hydrogen peroxide is about 1020 K, there would still be an overall plume cooling effect. Some residual hydrocarbon in the chamber exhaust plume appears to be essential in order to achieve significant reaction energy and thrust augmentation.

4.2 Thrust Augmentation using Helical Port Fuel Grains

Upon discovery of no noticeable increase in thrust using a cylindrical port, a helical port fuel grain was used. As demonstrated by Whitmore and Walker et al. [10], the helical-port fuel grain will substantially increase the fuel regression rate and lower the overall system's initial O/F ratio. This left more chemical potential energy in the core flow to react with the secondarily injected oxidizer. Once the decomposed peroxide is able to react with the fuel-rich core flow, the released heat enabled the remaining peroxide to react more freely. The helical fuel grain also spins the exhaust products, allowing for better mixing and slightly longer dwell time.

It can be seen visually in Fig. 4.4 that the nozzle pressure increased significantly due to secondary injection. The exit angle of the exhaust more than doubled with the secondary injection, indicating that the exhaust is more fully filling the nozzle. I can be seen in videos of these burns that the nozzle is separated, usually with the

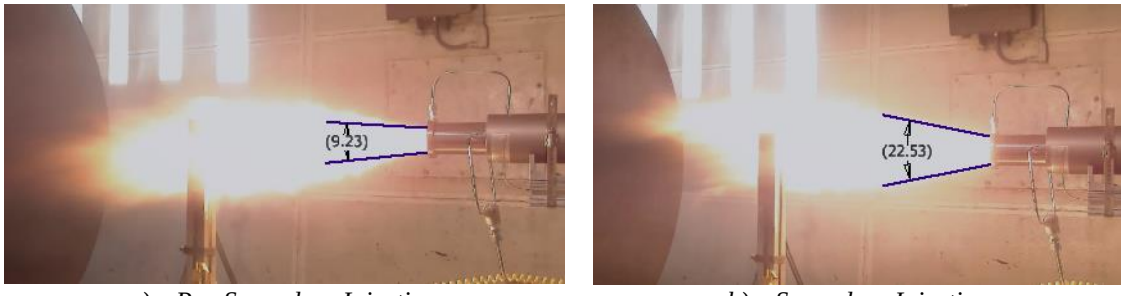

a) Pre-Secondary Injection *b) Secondary Injection*

Fig. 4.4 Visual of TAN injection with helical port (3/18/2019).

separation point shifting from the top to bottom. This caused the plume to vector in different directions. Once secondary injection commences, this shifting is dissipated and the separation voids can no longer be seen with the upstream facing camera. Clearly, the plume is no longer being cooled by the secondary gets noticeably hotter and the exit pressure is increasing, both common products of thrust augmentation.

Figure 4.5 shows the characteristic thrust and mass flow rate profiles. It will be noticed that the shape of the thrust profile is much different than that in Fig. 4.2. While this may seem to be caused by better internal combustion within the nozzle due to the effects of the helical fuel grain, it can be better attributed to the shifting O/F ratio. The helical fuel grain exhibited a much steeper O/F shift than what was seen from previous use with GOX [9, 10] (see Fig. 4.6). This can likely be attributed to use of an incompressible oxidizer which will self-regulate mass flow rate through injector-feed coupling and allow for a flatter chamber pressure while the O/F ratio is shifting dramatically. This is opposed to use of GOX as an oxidizer that will be choked at the injector and therefore not as sensitive to shifting O/F. During a 10 second burn, the O/F ratio was found to shift, nearly linearly with time, from below two to upwards of six or seven.

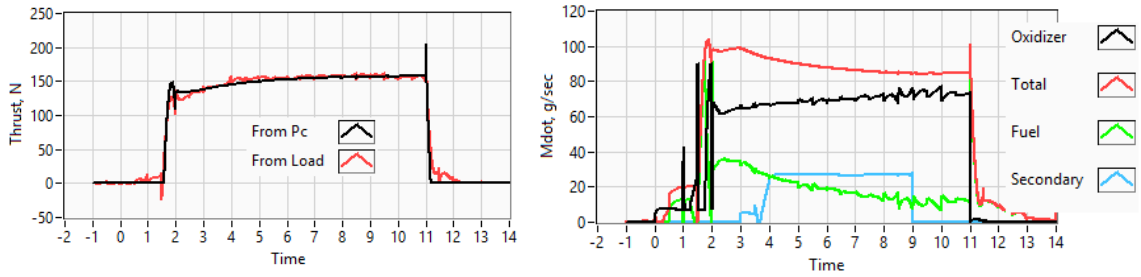

a) Thrust profile as measured directly and as calculated from chamber pressure

b) Mass flow rates of core flow and of secondary injection

Fig. 4.5 Thrust and mass flow rate of TAN injection with helical port (3/26/2019).

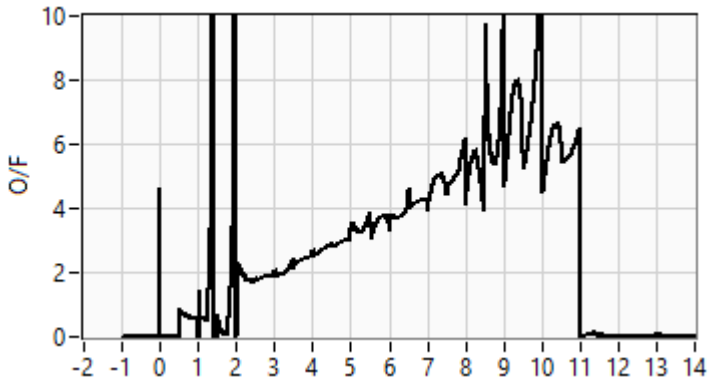

Fig. 4.6 Typical shifting O/F ratio of helical fuel port (3/26/2019).

4.3 Thrust Coefficient Augmentation

As a point of comparison, the change in thrust coefficient, ΔC_F, and augmentation ratio, AR, were calculated for each burn. Figure 4.7 summarized this result.

The trend line was added to characterize the general trend of thrust coefficient

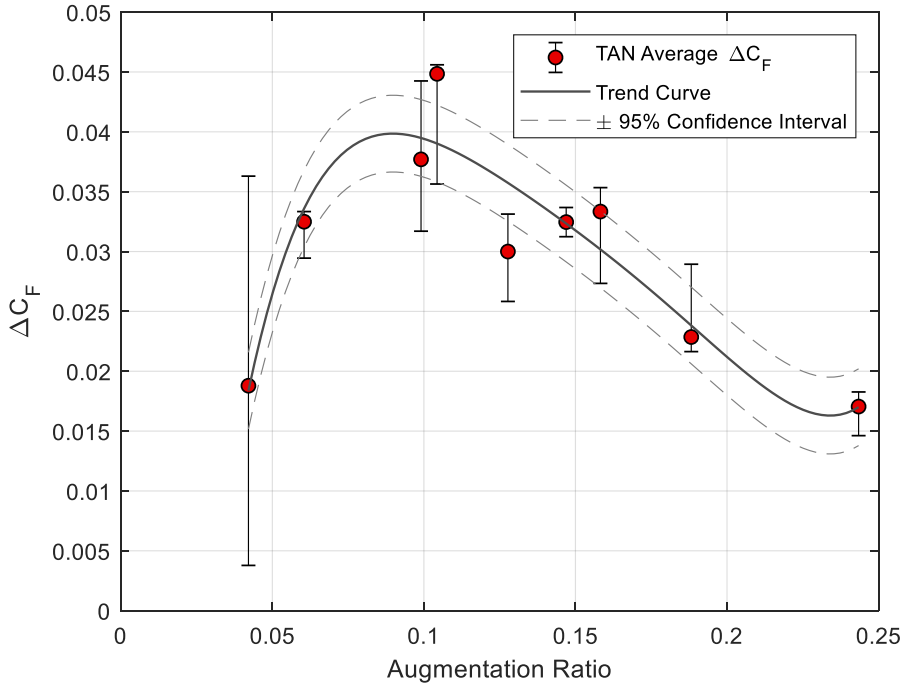

Fig. 4.7 Change in thrust coefficient vs. augmentation ratio.

with augmentation ratio. The 95% confidence interval is the confidence of the curve fit assuming a student-T distribution. The error bars on the data points were calculated based on the uncertainty of the analysis method, or in other words, the uncertainty of exact moment of when the thrust began to be augmented by the secondary injection.

The most notable characteristic of the data is that there exists a “sweet spot” at an augmentation ratio of about 0.9. Intuitively, the thrust should increase as more secondary propellant is added; however, this result may indicate that injecting more peroxide beyond a certain point does not allow sufficient dwell-time for full decomposition of the secondary flow, and results in a chilling effect on the exit flow. Up to the maximum point on Fig. 4.7 heat released from the peroxide decomposition / combustion of the peroxide is able to drive the liquid evaporation and increases thrust. However, once this “sweet spot” is passed, the liquid evaporation process becomes dominant and absorbs the needed enthalpy to drive decomposition.

4.4 Comparison of 1-D Decomposition Model with Test Data

Figure 4.8, Fig. 4.9, and Fig. 4.10 show results typical to the secondary injection process. The particular case shown includes results from a secondary injection mass flow rate of 15 g/s, a starting droplet diameter of 15 μm, and an O/F ratio of 5.

Figure 4.8 shows the mass flow rates of liquid and vapor. The liquid evaporates and becomes vapor, and the vapor decomposes and becomes a core flow product. In almost all cases the vapor flow rate reaches a maximum then decreases as the liquid evaporation rate decreases. If the simulation is more reaction limited, the gap between the decomposition curve and vaporization cure in Fig. 4.8b grows wider, whereas if it is

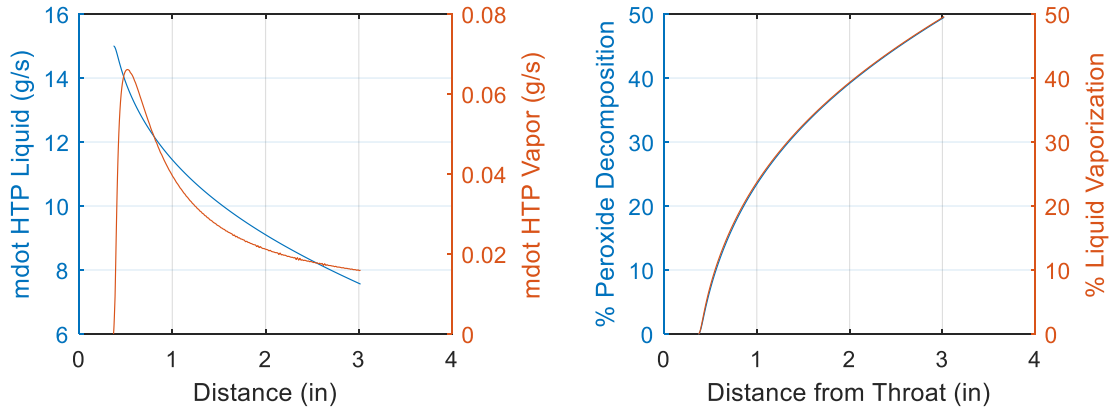

a) Mass Flow Rate through Control Volume. *b) Decomposition and Vaporization Percentage.*

Fig. 4.8 Typical HTP flow rates and decomposition percentage.

vaporization limited, as is likely the case for the TAN tests, then the curves nearly lie on top of each other.

Figure 4.9 shows the temperature and pressure profiles. Temperature, pressure, Mach, and velocity profiles presented here are consistent with the trend of addition to supersonic flow as outlined in Anderson [24]. This trend is outlined in Table 4.2.

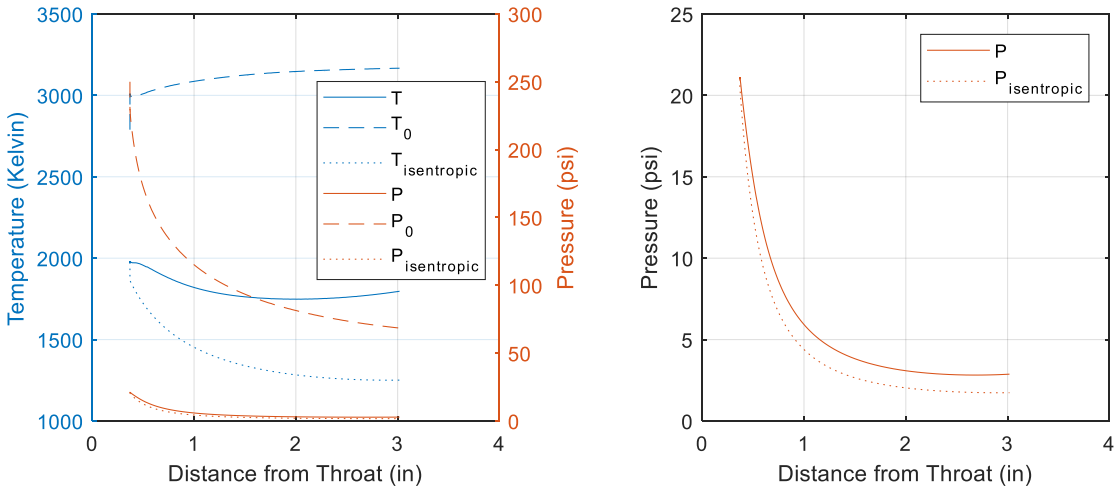

c) Temperature and Pressure Profile. *d) Pressure Profile Close-Up.*

Fig. 4.9 Typical temperature and pressure profiles, showing static, stagnation, and static isentropic values.

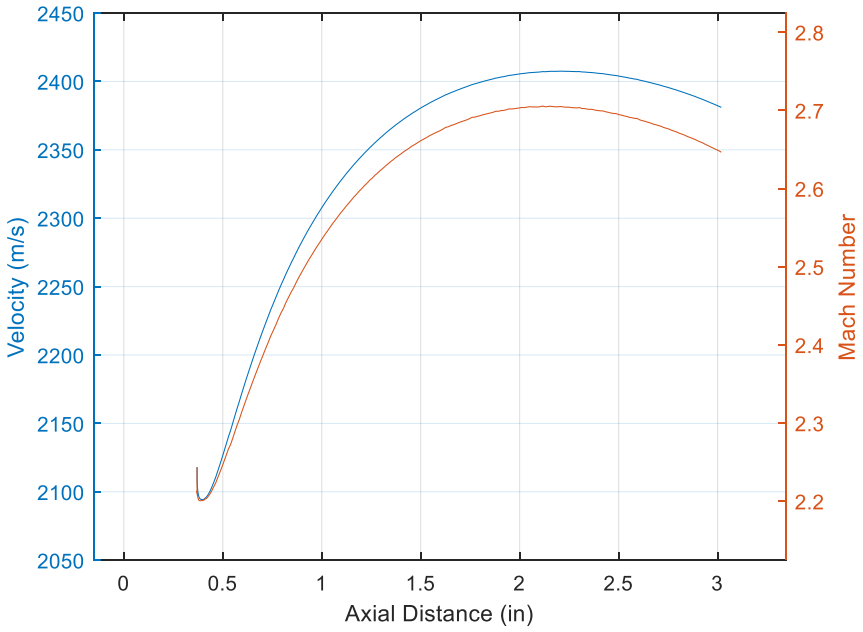

Fig. 4.10 Typical velocity and Mach number.

Table 4.2 Parameter changes in supersonic flow due to heat addition

Parameter	Change from Heat Addition
Mach Number	↓
Velocity	↓
Static Temperature	↑
Stagnation Temperature	↑
Static Pressure	↑
Stagnation Pressure	↓

Figure 4.11 presents the overall trend of the thrust coefficient for various initial droplet diameters. The model predicts a monotonically increasing augmentation effect, and does not demonstrate the “sweet” spot effect observed in the experimental data as presented in Fig. 4.7, and also overlaid on the same plot in Fig. 4.12 for convenience. This discrepancy could be for several reasons.

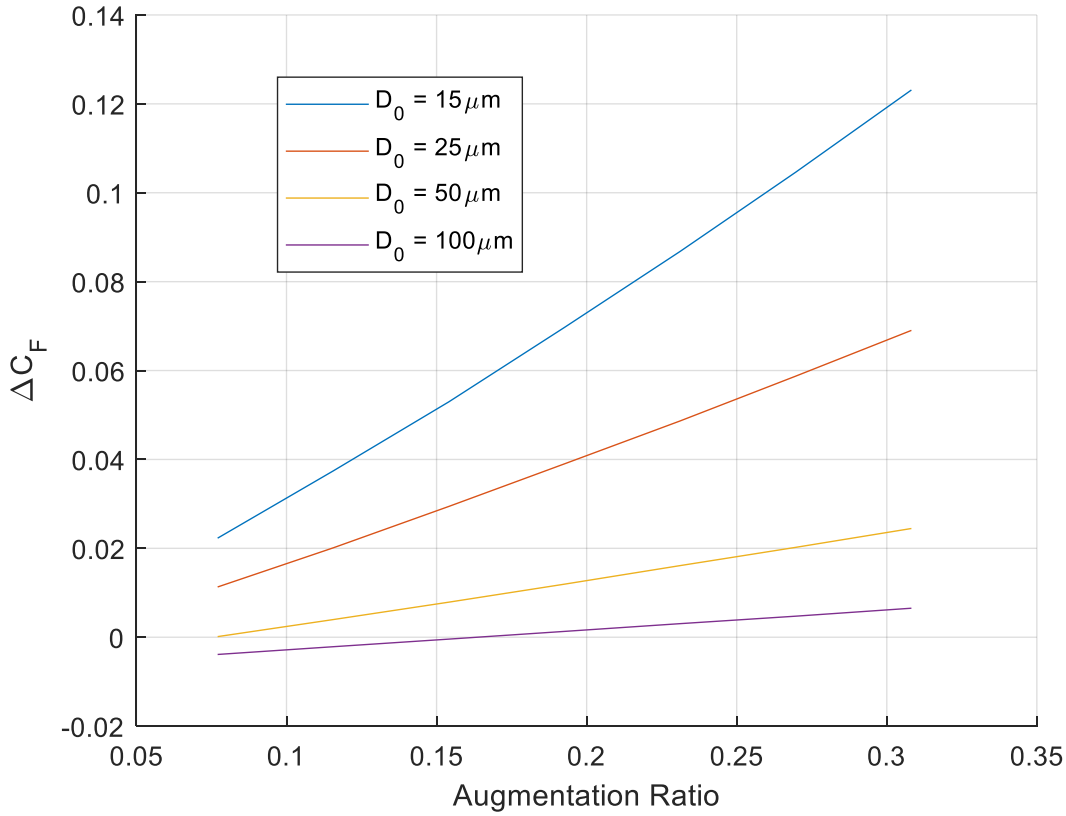

Fig. 4.11 Change in thrust coefficient vs. augmentation ratio for various initial droplet diameters.

First, the model does not account for mixing of the injected flow. The model assumes evenly dispersed droplets throughout the cross-sectional area of the nozzle. In reality, the liquid and secondary combustion products will stick to the nozzle wall more. This phenomenon would lead to localized effects that would significantly limit the actual evaporation and decomposition taking place. It is possible that better mixing happens with lower mass flow rates. Especially if the swirl effect of the helical fuel grain is significant for mixing. Higher secondary mass flow rates would effectively dissipate the angular velocity of the flow.

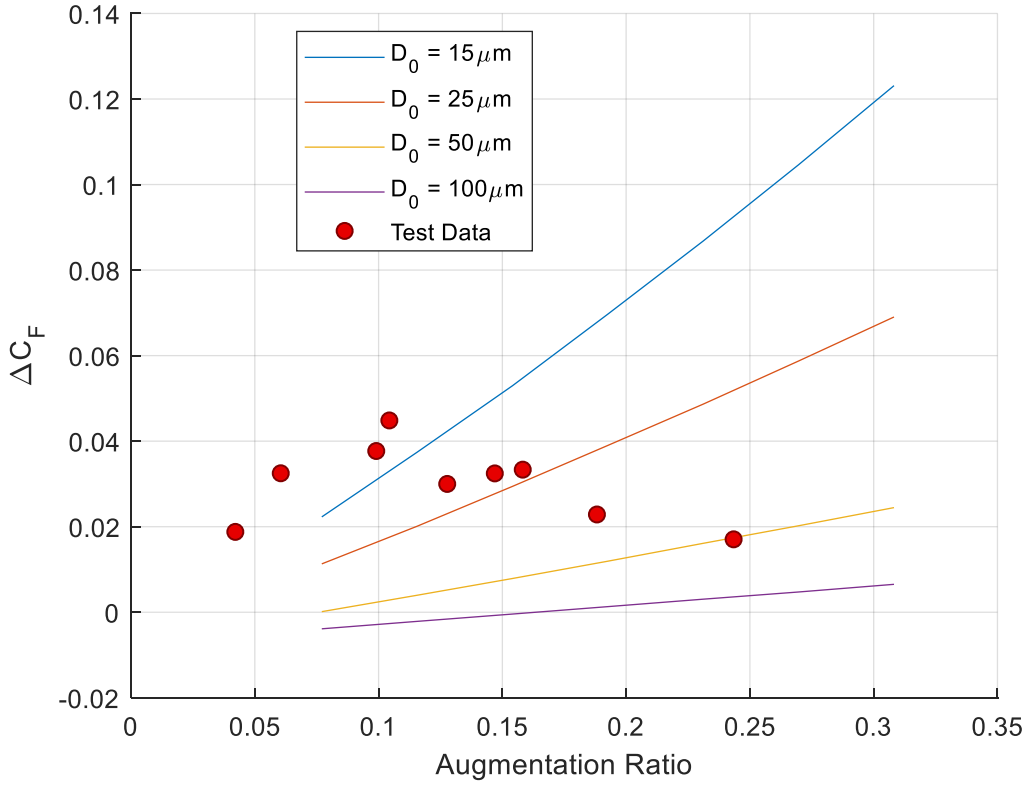

Fig. 4.12 Change in thrust coefficient vs. augmentation ratio for various initial droplet diameters with overlaid test data.

Second, a higher secondary mass flow rate would also cause a stronger oblique shock wave just upstream of the injection site. The stronger the shock wave or wider angle the shock wave has, the lower the thrust gains would be due to the secondary injection. In Fig. 4.13 the compression ratio is plotted against the augmentation ratio. Compression ratio is calculated using the procedure in section 2.4. Although it is not a very strong correlation, it does seem to have an upward trend with the augmentation ratio.

A final reason for this discrepancy could be the fact that the water and hydrogen peroxide were assumed to vaporize at the same rate in the model, where in reality water

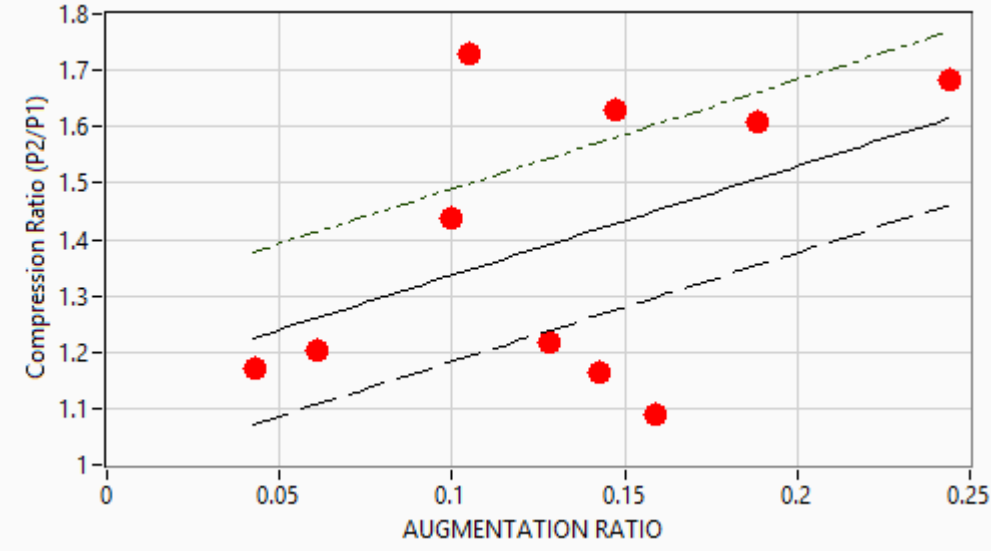

Fig. 4.13 Compression ratio as a function of augmentation ratio.

will vaporize preferentially to hydrogen peroxide, which makes the hydrogen peroxide preparation technique used in section 3.3 possible. Water evaporating at a higher rate than hydrogen peroxide would have a dampening effect on combustion, especially at higher mass flow rates.

Though the trend of the simulation does not show the trend observed in the data, it does have a similar magnitude, showing that although it is missing some physicality present during the tests, it does capture the overall picture of about how much decomposition and thrust augmentation is taking place, and can be used as a good first cut to determine the proper nozzle length to have sufficient thrust augmentation to work for altitude compensation.

Figure 4.14 shows a stronger correlation between test data and computer model results. This figure suggests that the initial diameter was more consistent across tests assuming other unknown parameters remained constant. Figure 4.15 shows the typical

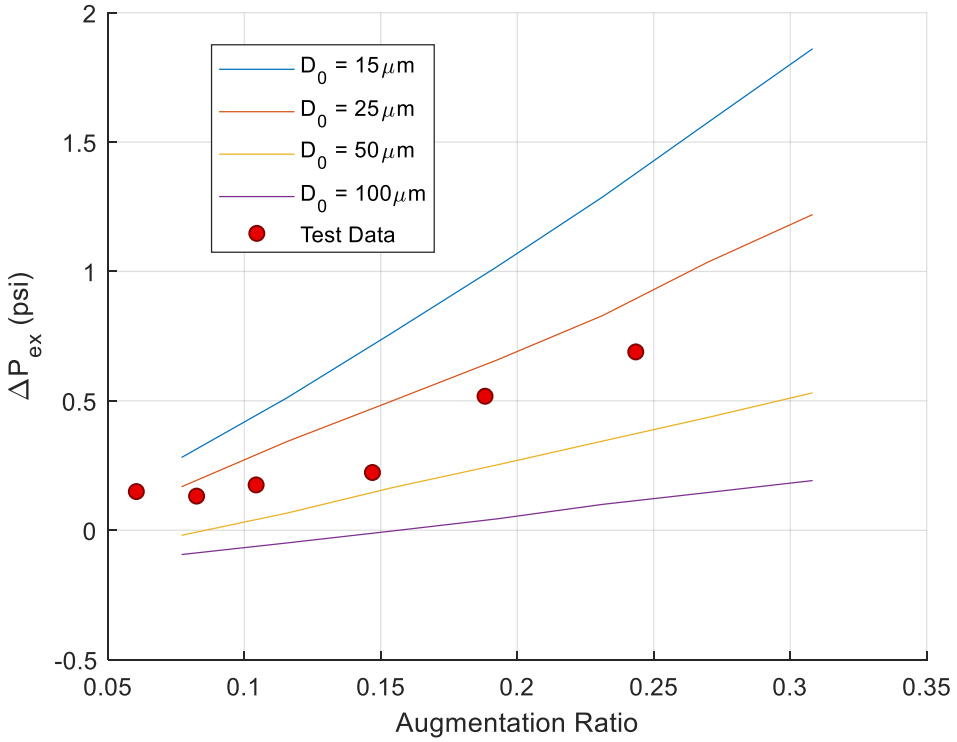

Fig. 4.14 Change in exit pressure test data overlaid on computer model results.

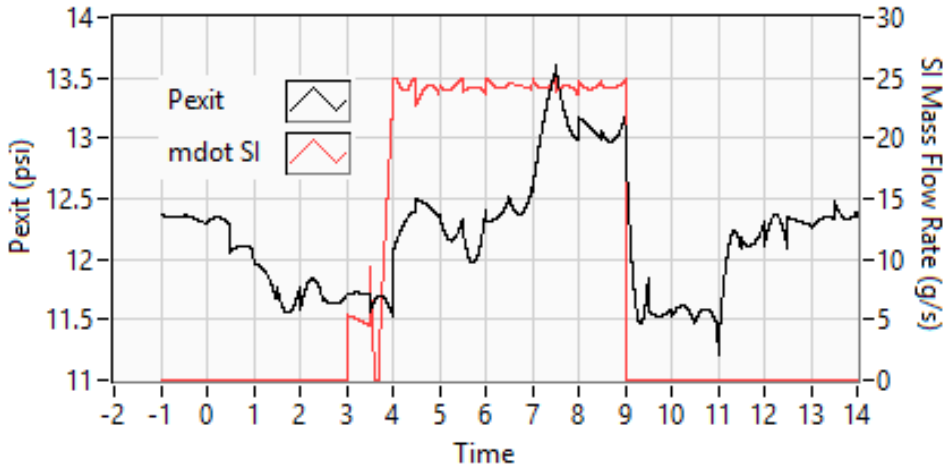

Fig. 4.15 Exit pressure and secondary injection mass flow rate (3/26/2019).

exit pressure history for a TAN test. The isentropic exit pressure is less than 2 psia, showing that flow is separated at the exit pressure port. The data in Fig. 4.14 assumes that a change in pressure at the exit pressure port is equivalent to the change in pressure of the nozzle centerline.

Figure 4.16 shows that decomposition percentage increases with added mass flow, suggesting that with adequate mixing additional secondary injection would increase reaction rate and reduce dwell time. It should be noted that if this is pushed to the extreme, there is an upper limit as to how much could be injected due to thermal choking.

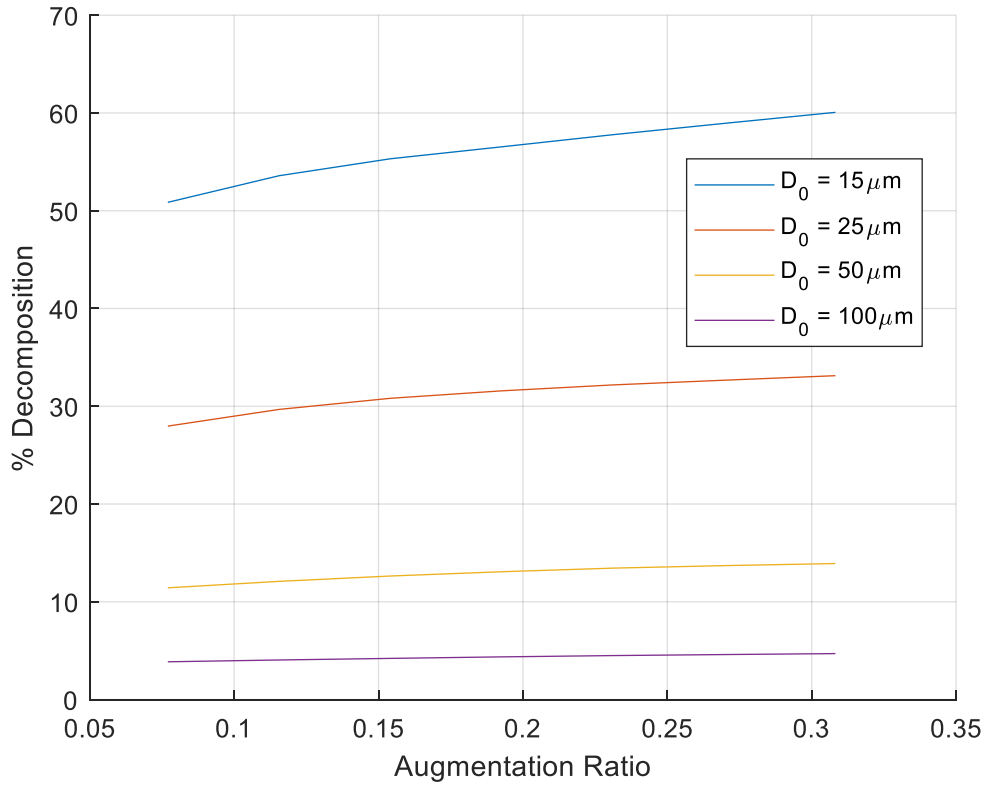

Fig. 4.16 Decomposition percentage as a function of augmentation ratio at varying initial droplet diameters.

Figure 4.17 shows the impact of initial droplet size on TAN performance. In several cases, if the droplet size was too large, the core flow could not sufficiently vaporize the droplets leading to a decrease in thrust. The droplet sizes analyzed are in the range of droplet sizes typically used in supersonic combustion simulations [6, 19], and given the magnitude of ΔC_F found in Fig. 4.11 and Fig. 4.12, represent the range of droplet sizes experienced in the TAN test fires. Clearly minimizing droplet size is vital for efficient TAN operation with finite-length nozzles.

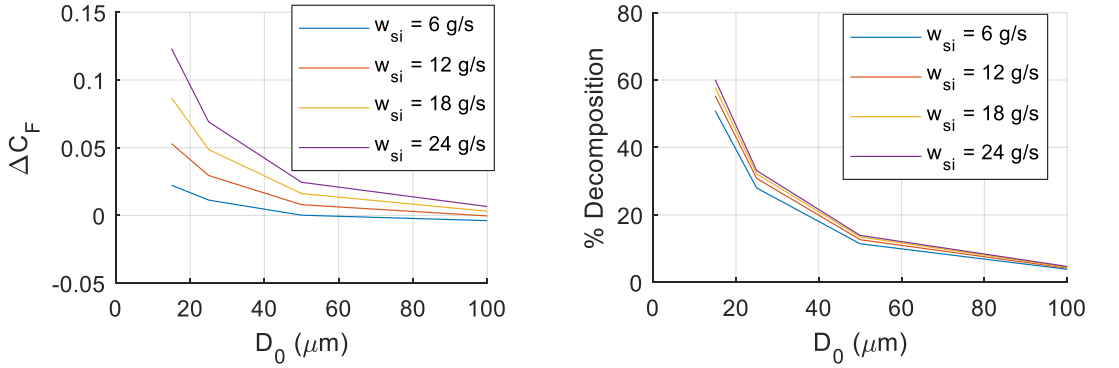

a) Thrust Coefficient vs. Initial Droplet Size. *b) Decomposition Percentage vs. Initial Droplet Size.*

Fig. 4.17 Effects of initial droplet diameter on thrust coefficient and decomposition.

4.5 Sensitivity Analysis of Kinetic Decomposition Model

The magnitude of the influence that each dependent variable, such as change in mass flow rate, inflicts of each depended variable, such as change in temperature, is summarized by Fig. 4.18 and Fig. 4.19.

The change in cross sectional area has the largest influence on all parameters. For parameters in which the change in energy is important, the higher the influence the better for TAN applications. The influence on temperature is of particular interest. If the energy

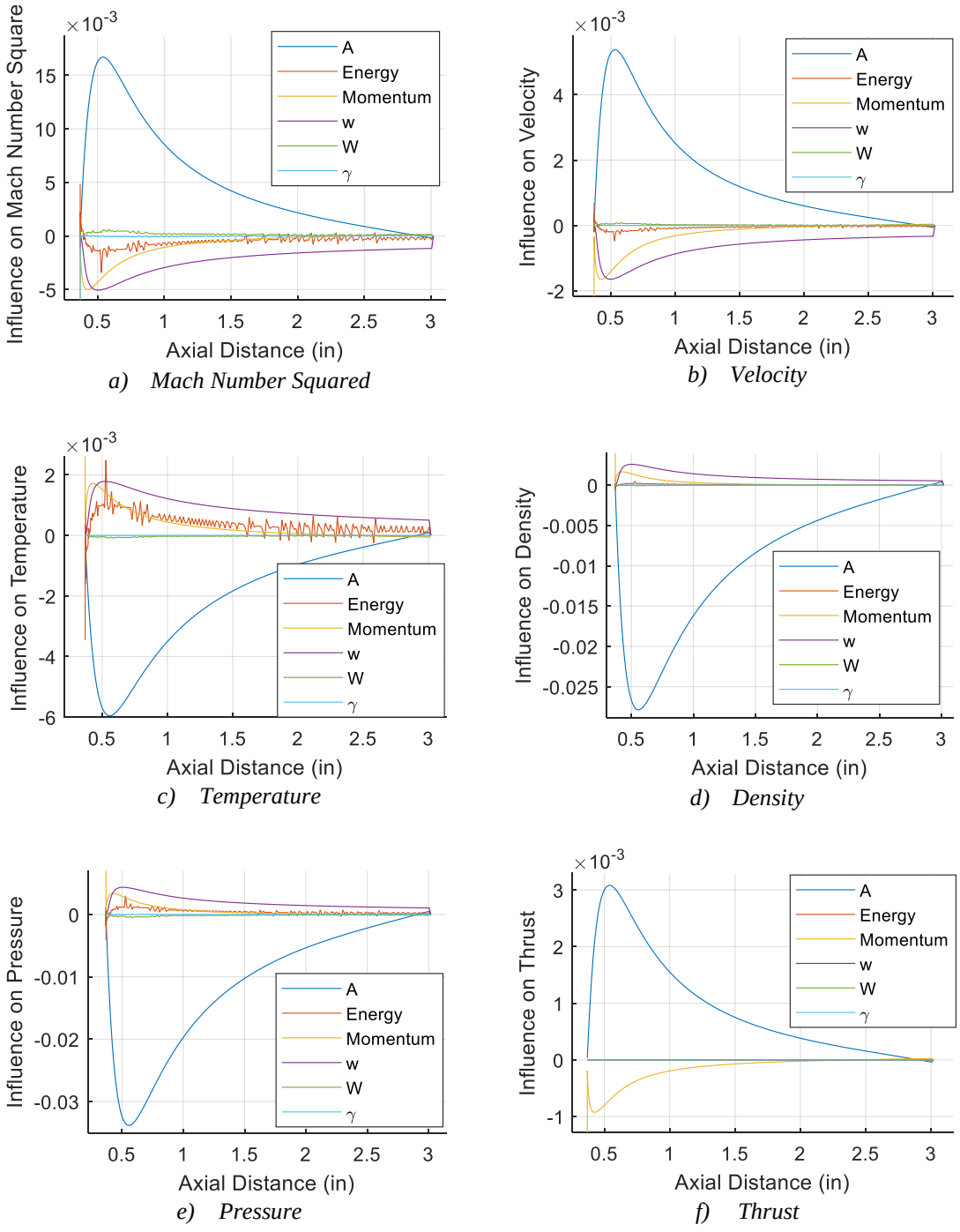

Fig. 4.18 Effect of influence coefficients on select parameters.

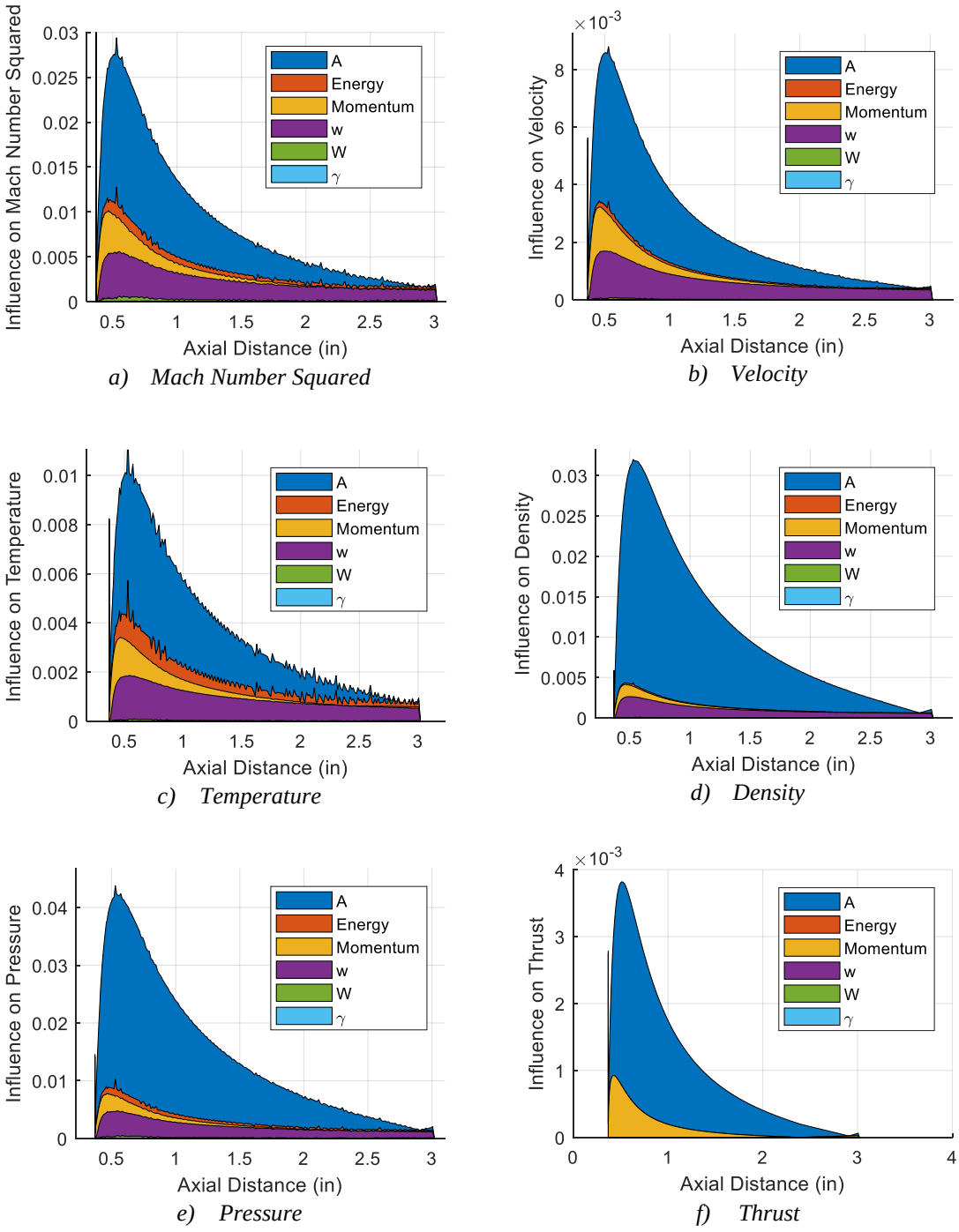

Fig. 4.19 Summation of the magnitudes of influence coefficients on select parameters.

term is able to overpower the mass flow and momentum terms, the temperature will have a greater increase with less momentum losses. This translates to more energy input possible before reaching a maximum, where thermal choking occurs. The way to make the energy term more dominant is by injecting secondary propellant with a higher energy density. This means propellants that translate to higher I_{sp} gains. This is an obvious limiting factor for injecting oxidizer only since the energy density is much lower than if a bi-propellant system would use. Increased complexity is a drawback of a bi-propellant system and the monopropellant TAN system used here could compensate for the lower energy density with lower complexity.

The instabilities in the influence of the change in energy seen in Fig. 4.18 and Fig. 4.19 is due to the nature of determination of the combustion energy. The enthalpy of formation of the combustion reactants and products was used to determine the heat of combustion. When using small step sizes, the CEA results seemed to be near machine precision, which propagated to the wiggles seen in Fig. 4.18 and Fig. 4.19.

4.6 Optimization Analysis

In the TAN test campaign using hydrogen peroxide as the secondary propellant, very small increases in thrust were seen due to incomplete secondary combustion. In this section, the required length and dwell time for complete secondary combustion will be determined. The optimal configuration for the TAN system will also be explored. For consistency, conditions for the test site, Logan, UT will be used in the optimization cases.

Assuming an infinitely long nozzle, or a nozzle in which all peroxide has reacted, results were generated for O/F ratios of 3 and 5. These O/F ratios were chosen as they

showed higher performance enhancement than other considered O/F ratios. These results are presented in Fig. 4.20 through 4.25.

The weighted specific impulse used in Fig. 4.21 and Fig. 4.24 was determined using a formula recommended by Forde [3]. It uses an 80/20 rule, assuming 20% sea-level I_{sp} and 80% vacuum I_{sp}, which was based on previous studies of two-stage to orbit trajectories. This helps demonstrate the effects of TAN throughout a mission. The sea-level I_{sp} is calculated with TAN on, and the vacuum I_{sp} is calculated with TAN off. The optimal unaugmented ratios were calculated using this criterion, 11.2 for O/F = 3, and 12. 2 for O/F = 5.

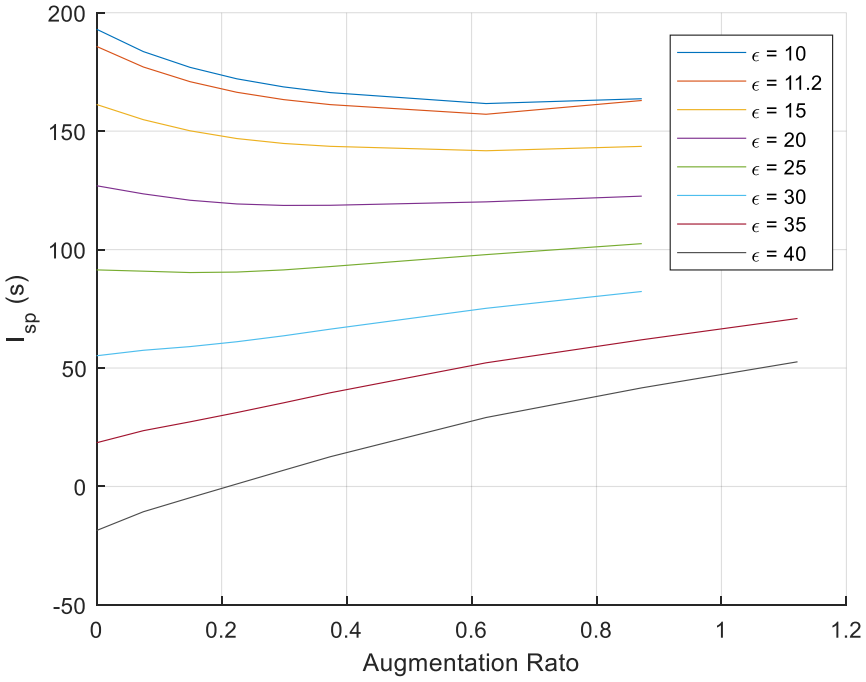

Fig. 4.20 Specific impulse of an infinitely long nozzle, O/F = 3.

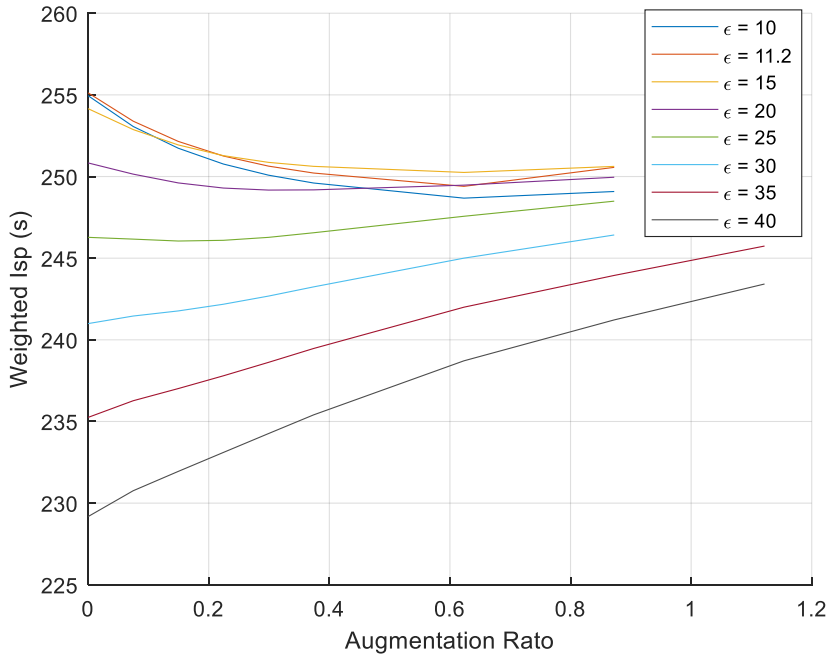

Fig. 4.21 Weighted specific impulse of an infinitely long nozzle, O/F = 3.

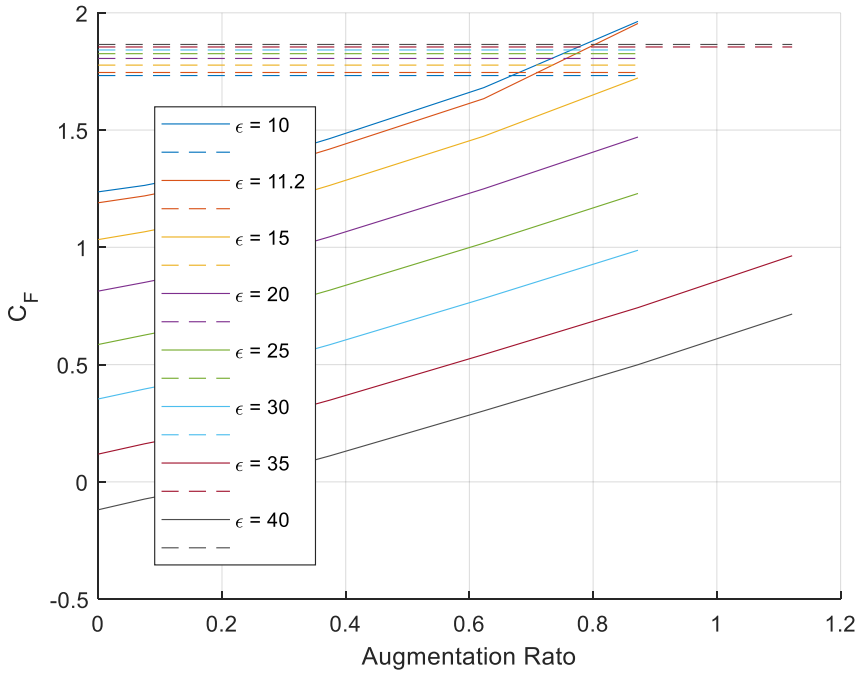

Fig. 4.22 Thrust coefficient of an infinitely long nozzle, O/F = 3.

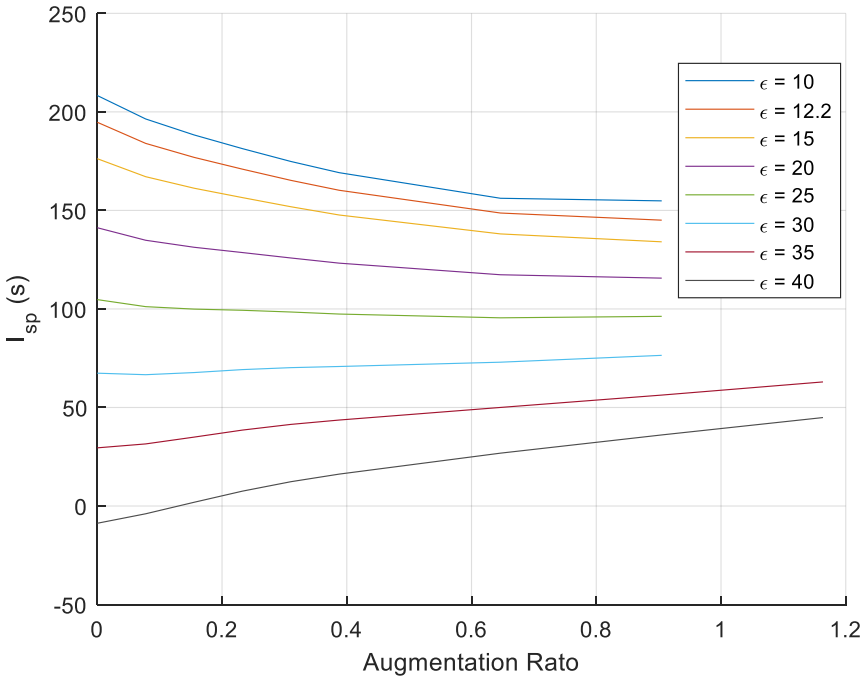

Fig. 4.23 Specific impulse of an infinitely long nozzle, O/F = 5.

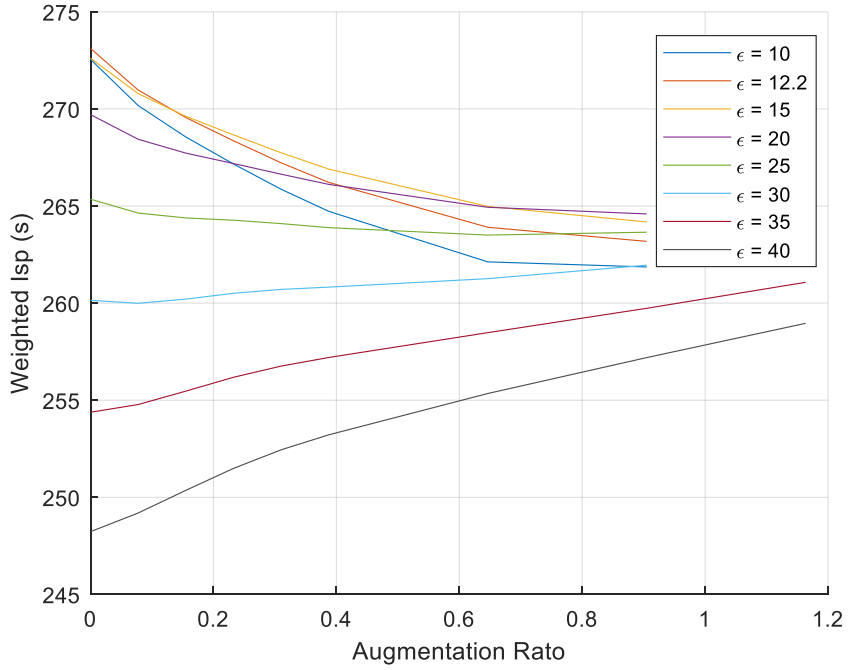

Fig. 4.24 Weighted specific impulse of an infinitely long nozzle, O/F = 5.

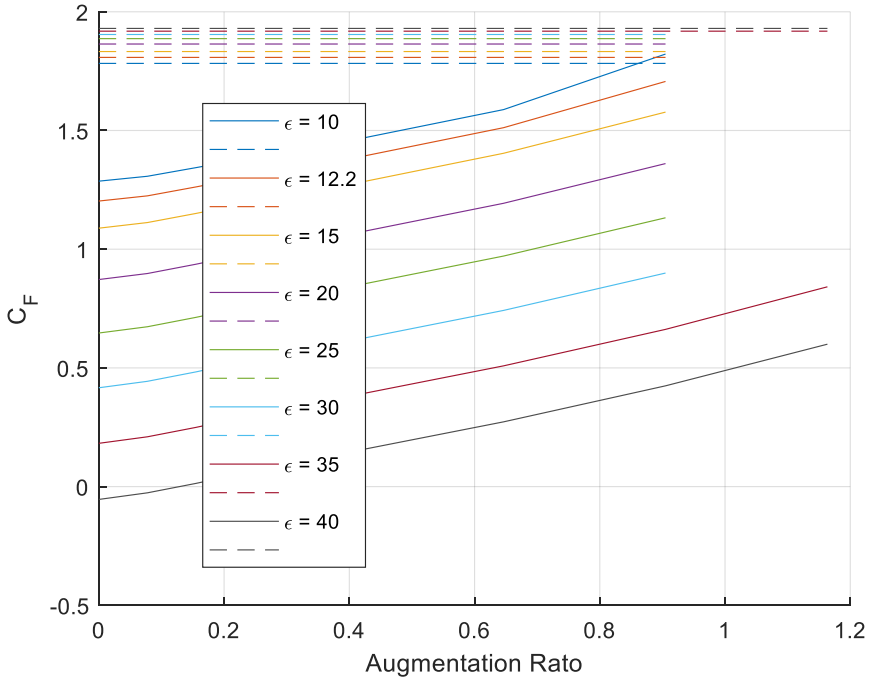

Fig. 4.25 Thrust coefficient of an infinitely long nozzle, O/F = 5.

As can be seen in Fig. 4.20 and Fig. 4.23 that at very high expansion ratios, secondarily injected hydrogen peroxide can improve I_{sp} above the case using the same expansion ratio with no secondary injection. This effect is magnified the higher the expansion ratio. The mission-weighted I_{sp} in Fig. 4.21 and Fig. 4.24 shows an increased upward trend as augmentation ratio increases. However, in neither the O/F of 3 or 5 cases was the mission averaged specific impulse shown to improve with use of TAN over the unaugmented optimal expansion ratios. Bases on the upward trend of weighed I_{sp} with augmentation ratio, it seems likely that if it were possible to inject more propellant, than the I_{sp} could be driven beyond the unaugmented optimal values. The limiting factor is onset of thermal choking. If it were possible to stage injection in such a way that heat release is controlled, then more propellant could be added and possibly surpass the

maximum value. Another way to increase the I_{sp} would be to added higher energy oxidizers, or as was shown by Refs. [2, 3], fuel and oxidizer could be injected.

Even without an increase in sea-level or mission-averaged specific impulse, TAN can still be useful. Fig. 4.22 and Fig. 4.25 show how the thrust coefficient is augmented with secondary injection. If a reasonable expansion ratio were used, then the lift-off thrust could be greatly increased with TAN with only a marginal loss in specific impulse. This would mean that TAN is being used more as a lightweight secondary booster. By applying TAN at the beginning of the launch phase, the thrust is dramatically increased where added thrust is most needed, and then is turned off once the atmosphere is thinner and gravity losses not as significant. For the O/F = 3 case, if the mission-averaged optimal expansion ratio of 11.2 were used, then the sea-level thrust could be augmented by more than 60%, with a drop of only 4 seconds of mission averaged I_{sp}. For the O/F = 5 case, the mission-averaged optimal expansion ratio of 12.2 still gives about the best case with an increase in sea-level thrust over 40% and a drop-in mission averaged I_{sp} of about 10 seconds.

The required nozzle length and dwell time was determined from select cases of complete decomposition and with knowledge of the general evaporation behavior of droplets. As suggested by Turns [29], theoretically droplets should follow the D^2 law.

As shown by Fig. 4.26, the D^2 law states that the time derivative of the square of the droplet diameter is constant. In our case the slope is not quite constant, but it is nearly linear.

The evaporation constant, K, is calculated for constant slope as follows:

$$K = \frac{D_f^2 - D_0^2}{t} \tag{4.1}$$

Here D_0 and D_f are the initial and final droplet diameters, respectively, and t is the droplet evaporation time. The evaporation constant calculated for the initial diameter cases shown in Fig. 4.27 are nearly equal. This is consistent this the D^2 law. The evaporation rates of droplets are path dependent, meaning that the droplet evaporates differently at different points in the nozzle due mainly to changing nozzle area. Since both cases shown in Fig. 4.27 use the same contour, just stretched to the correct size, their evaporation constants are the same.

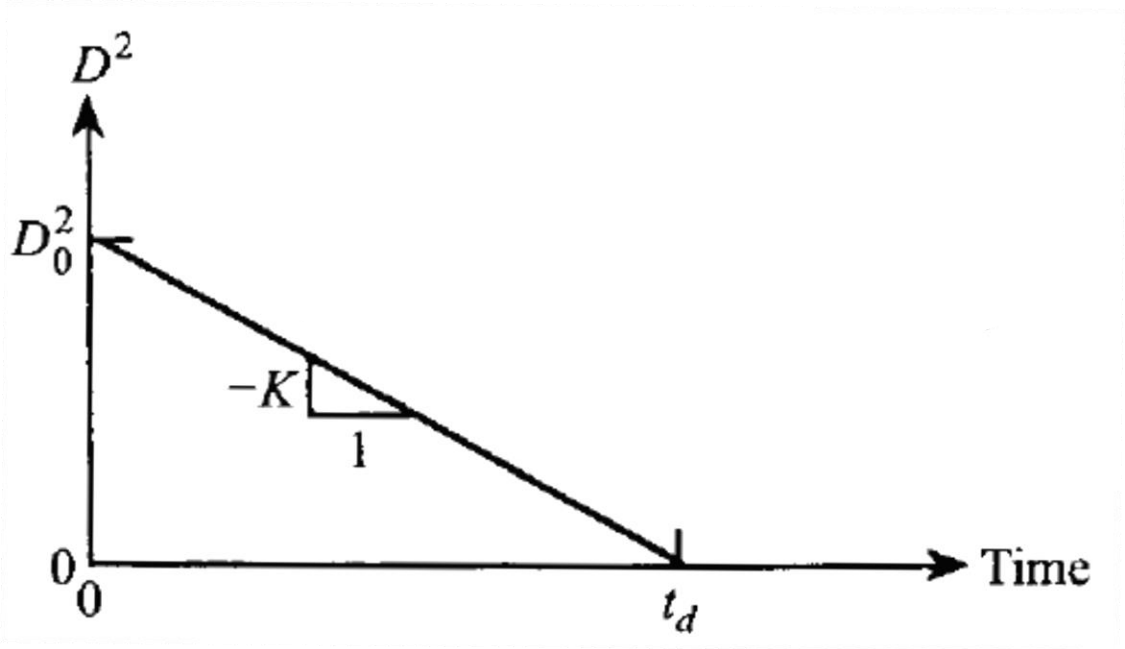

Fig. 4.26 The D^2 law.

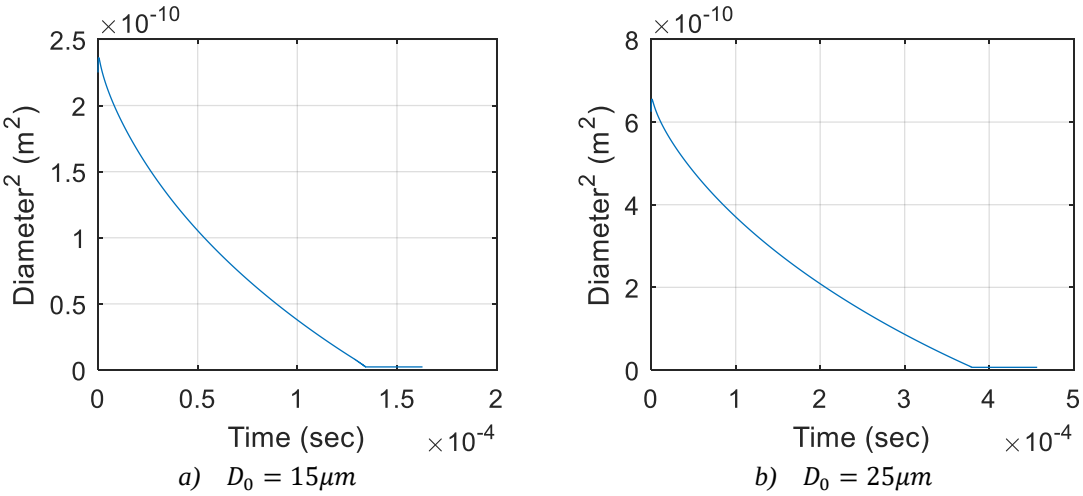

a) $D_0 = 15\mu m$ *b)* $D_0 = 25\mu m$

Fig. 4.27 The similar shape of the D^2 curve.

The secondary mass flow rate theoretically also has very little impact on the evaporation coefficient, as seen in Fig. 4.28. The plot legends have been taken off since there is little distinguishable difference between curves, but each curve is for a different secondary mass flow rate. Figure 4.28 shows great variance with different initial diameters. This is largely due to the fact that evaporation was not completed. Since the evaporation rate is path dependent, the evaporation constants are greatly different for the partial evaporation cases.

Based on the assumption that the evaporation constant is independent of diameter and secondary mass flow rate, the largest influence on the constant is the temperature, which is strongly correlated with the O/F ratio. Table 4.3 summarizes the evaporation coefficients of several cases.

Obviously, there is a very strong correlation with initial droplet diameter and O/F ratio. To achieve minimum dwell time, stoichiometric mixture ratios should be used and the initial droplet diameter should be made as small as possible. Based on these, a

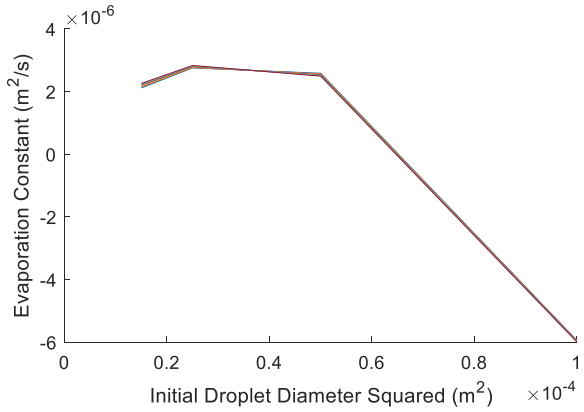

a) O/F = 4.

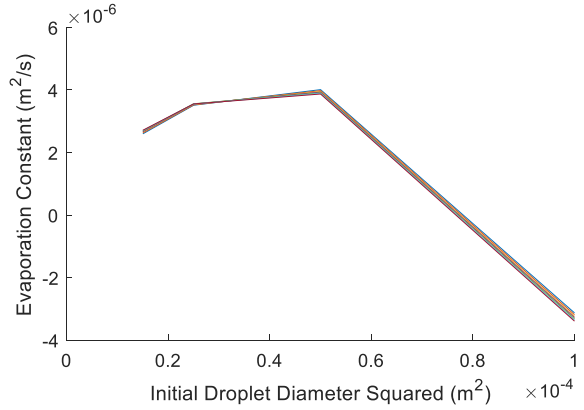

b) O/F = 5.

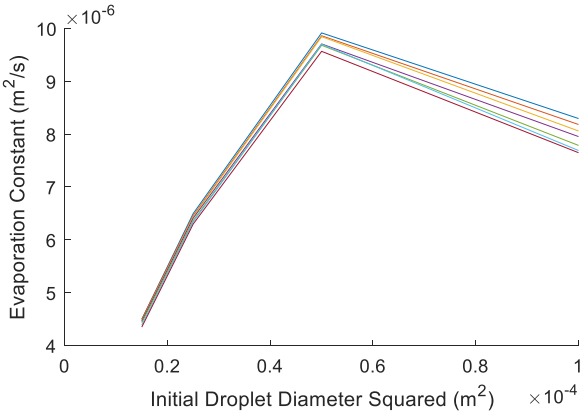

c) O/F = 7.

Fig. 4.28 The evaporation constant is constant with flow rate.

Table 4.3 Parameters for required nozzle length and dwell time

O/F Ratio	Mass Flow Rate (g/s)	Initial Droplet Diameter (μm)	Evaporation Constant (10^{-6} m^2/sec)	Required Dwell Time (10^{-3} sec)	Required Nozzle Length (in)
3	12	15	0.90680	24.813	24.53
3	24	15	1.0922	20.6	20.5
5	12	15	1.5110	14.891	15.83
5	24	15	1.6760	13.425	12.61
5	24	25	1.6465	37.959	35.54

required nozzle length should be predictable. In this idealized analysis, the relative size of the nozzle doesn't matter as long as the expansion ratio and nozzle length are similar, since exhaust velocity and temperature are only a function of area ratio and not core mass flow rate.

The results summarized in Table 4.3 reflect the results of the computer model and not necessarily that of test data, as shown with the discrepancy in Fig. 4.12. Likely there is an unmodelled parameter that would increase actual required dwell time. These results are intended for reference only and further testing is needed for verification.

4.7 Explosive Instabilities of Cold Hydrogen Peroxide

Hydrogen peroxide has long been used as rocket propellant in both mono-propellant and bi-propellant applications. Typically, a catalyst is used to initiate or sustain hydrogen peroxide decomposition. Much less commonly, hydrogen peroxide is decomposed thermally. While this has the advantage on eliminating the need for the expensive dead weight of a catalyst bed, it comes with its own problems. Thermal decomposition of hydrogen peroxide tends to exhibit chamber pressure instabilities.

During the TAN test campaign, two explosions occurred during static hot fires.

These explosions both occurred very shortly after injection of hydrogen peroxide commenced. It is believed that these explosions can be attributed to the cold test conditions, 6°C and 0°C. This statement will be defended after looking at other examples of instability.

ONERA, a French aerospace company, developed a hydrogen peroxide/HDPE hybrid rocket that used pyrotechnics to initiate thermal decomposition of hydrogen peroxide [28]. When using a coarse atomizing injector, they experienced significant instabilities in chamber pressure. When they switched to a very fine droplet atomizer, the instability was significantly reduced. They also used a catalyst bed for later tests and reported no stability issues.

Whitmore [11] experienced significant combustion instability when using an oversized injector. These instabilities were alleviated once the injector had been replaced by a smaller orifice injector. The smaller injector provided a larger pressure drop, which decreased the pressure coupling of the system. Another reason this may have improved stability is due to the smaller injector providing better atomization. As the pressure drop across the injector increases, the atomization characteristics increases.

In both cases the instability was improved by decreasing the droplet size of injected hydrogen peroxide. Hydrogen peroxide exhibits a transient behavior called “pooling” where it will collect until it has gained enough energy to decompose, at which point it quickly raises the chamber pressure, decreasing oxidizer flow. The decreased oxidizer flow causes chamber pressure to drop, the oxidizer flow to increase, pool, and repeat. This frequency is driven down and the amplitude driven up by increasing the time

required to vaporize and decompose the peroxide. As seen in previous results of hydrogen peroxide vaporization in supersonic flow, the larger the droplet size and the colder the liquid, the longer vaporization and decomposition takes.

Both ONERA and Whitmore experience instabilities due to increasing the time required to decomposed the injected peroxide. The explosions experienced during TAN test were likely due to a similar phenomenon of increasing required decomposition time. The test apparatus was exposed to the coldest temperatures that had yet been experienced during two peroxide test fire campaigns. The test the day of the warmer temperature of $6°C$ had been delayed and the test cart remained in the cold for an unusually long time and became cold soaked. After the two explosions happened, precautions were made to ensure the peroxide flow path remained warm. No further instabilities were experienced due to cold conditions.

It should be noted that colder temperatures do not seem to affect the performance of hydrogen peroxide hybrid rockets that use catalyst beds. As already stated, ONERA experienced no stability issues with their cat bed configuration. Nammo also developed a hydrogen peroxide hybrid rocket [30]. During testing of their hydrogen peroxide/HTPB rocket, they performed a cold test where they cooled the test apparatus to $-17°C$. This is right at the freezing point of peroxide. Using their catalyst bed, they experienced no instabilities, only lowering their chamber pressure slightly due to lower flame temperature.

The sensitivity of hydrogen peroxide thermal decomposition hybrid rockets to cold conditions reveals a significant shortcoming of the system. If this ignition system

were to be used for in space propulsion, sub-zero temperatures are easily reached. Solutions to this problem include warming the lines as was done during the tests, or using a catalyst bed to sustain decomposition. Heating lines is very expensive in terms of weight and energy. Catalyst beds have drawbacks discussed earlier, but seem like the better solution. More testing is needed to better characterize sensitivity to cold on thermal decomposition of hydrogen peroxide.

CHAPTER 5

CONCLUSIONS AND FUTURE WORK

A hydrogen peroxide injected thrust augmenting nozzle concept has been tested and analyzed. The reported TAN design retrofits an existing hybrid rocket system burning a 90% solution of Hydrogen Peroxide and Acrylonitrile-Butadiene-Styrene (ABS) as propellants. The design leverages 3-D additive manufacturing to embed a helical fuel port into the thrust chamber of a hybrid rocket burning hydrogen peroxide and ABS as propellants. Previous studies using GOX as a secondary injectant have been shown to increase thrust with sufficiently fuel-rich core flow. While this worked well as a means of increasing the thrust of the down-tuned hybrid rocket, it was desired that this dependency on fuel-rich core flow be mitigated. As a solution, hydrogen peroxide replaced GOX for both the main flow oxidizer and secondary injectant. Hydrogen peroxide undergoes an energetic decomposition when heated to high temperatures and works well as a high-density oxidizer.

The thrust augmenting nozzle used in the previous TAN test campaign was retrofitted to an existing hydrogen peroxide/ABS hybrid rocket. Application of hydrogen peroxide to the TAN was shown to improve thrust through a series of static hot-fire tests. An increase in thrust was detected using load-cell measurements and comparing that value to baseline cases. Secondary combustion was also evident based on plume observations. The angle of gases as they escaped the nozzle increased with secondary injection, showing that there was an increase in nozzle pressure.

The effects of thrust augmentation were explored for various flow rates and

expansion ratios assuming an infinite nozzle length. It was found that the effects of secondary injection become more pronounced with higher expansion ratios. At higher expansion ratios, larger than 25:1, sea-level specific impulse increases with added secondary mass flow. When looking at mission averaged specific impulse, it was found that significant increases in thrust could be obtained using secondary injection with only minimal losses in specific impulse.

While a definite increase in thrust was measured, the increase was far less than that found in theory. This deficiency was found to be due to an insufficient dwell time in the rocket nozzle. According to a decomposition and combustion kinetic model, the peroxide was calculated to be somewhere between 70% maximum and 5% minimum. The test data showed that a "sweet spot" existed at a secondary mass flow rate of about 10 to 11 g/s or and augmentation ratio of about 10%. At higher mass flow rates, the energy required to vaporize the peroxide began to overpower the combustion reaction. This dwell time issue is easily mitigated by increasing the nozzle length. According to the model, a nozzle length on the order of a foot could be sufficient to vaporize and decompose all peroxide given a small enough initial droplet diameter and adequate mixing.

Increasing the length of the nozzle, while the simplest solution, may be less feasible than other options. In dwell time studies, it was found that the required nozzle length for full decomposition could be in excess of three feet, depending on degree of droplet atomization achieved. This would work for larger launch configurations, but not as well for smaller launch vehicles. Droplet size can be decreased using smaller injectors.

This would also increase penetration and mixing.

The author recommends more testing of the TAN system using a longer nozzle. Using a nozzle that is long enough to ensure complete vaporization and decomposition given perfect mixing, the effects of injector configurations could be explored. Billing [31] states that the optimal configuration for supersonic combustion is one where the combustor has a sonic exit. This is the maximum amount of propellant that can be added. It was found that at a sufficiently high expansion ratio the specific impulse will be increased with added propellant. Driving the nozzle exit to Mach one or close to it requires that no thermal choking happen before (or at) the exit. This requires fine tuning of the heat release mechanism. This could be tuned by injector location, orientation, and size. Significant work would need to be done to ensure complete vaporization and combustion at high secondary flow rates without prematurely driving the flow to Mach one. This would be necessary to increase its test readiness level and get closer to flight ready status.

As stated earlier, more research and testing needs to be done on the thermal ignition and decomposition system used for the TAN motor and its sensitivity to cold conditions.

This study has shown the feasibility of the hydrogen peroxide injected thrust augmenting nozzle and its limitations. The main limitation for this application was found to be dwell time and nozzle length. Significant thrust augmentation using hydrogen peroxide is not attainable using the three in long nozzle that was used in the test campaign. Remedies to this include increasing the nozzle length, providing better

atomization of injected propellant, or using a catalyst to initiate decomposition and vaporization. Thrust augmentation with hydrogen peroxide has the ability to act as an altitude compensating nozzle and as a built-in rocket booster. Increased thrust due to secondary injection has been demonstrated. With sufficient follow-up testing and engineering the hydrogen peroxide injecting thrust augmenting nozzle has the potential to revolutionize the launch vehicle industry.

REFERENCES

[1] G. P. Sutton and O. Biblarz, *Rocket Propulsion Elements, 7th ed.,* Wiley, New York, 2001, pp. 68-77. ISBN 9788126525775. https://pdfs.semanticscholar.org/6cce/fa84a00b396c5b50b66063772f4851392b8f.pdf

[2] Bulman, M. J., "Thrust Augmented Nozzle (TAN): The New Paradigm for Booster Rockets," AFRL-PR-ED-TP-2006-195, *42nd AIAA/ASME/SAE/ASEE Joint Propulsion Conference*, Sacramento, CA, 9-12 July 2006. https://apps.dtic.mil/dtic/tr/fulltext/u2/a454615.pdf

[3] Forde, S., Bulman, M., Neill, T., "Thrust Augmentation Nozzle (TAN) Concept for Rocket Engine Booster Applications," *Acta Astronautica*, 59 (2006) 271-277, Aerojet, Sacramento, CA, 2006. https://doi.org/10.1016/j.actaastro.2006.02.052

[4] Woodberry, R. F. H., Zeamer, R. J., and Keller Jr., R. B., "Liquid Injection Thrust Vector Control (LITVC)," *Solid Rocket Thrust Vector Control*, NASA SP-8114, Cleveland, Ohio, 1974, pp. 70-74. http://hdl.handle.net/2060/19760010106

[5] Borowski, S. K., Corban, R. R., Culver, D. W., Bulman, M. J., McIlwian, M. C., "A Revolutionary Lunar Space Transportation System Architecture Using Extraterrestrial LOX-Augmented NTR Propulsion," AIAA-94-3343, *30th AIAA/ASME/SAE/ASEE Joint Propulsion Conference*, Indianapolis, IN, 27-29 July 1994. https://doi.org/10.2514/6.1994-3343

[6] Zhu, L., Luo, F. Qi, Y. Wei, M., Ge, W. Liu, W. Li, G., Jen, T., "Effects of Spray Angle Variation on Mixing in Cold Supersonic Combustor with Kerosene Fuel," *Acta Astronautica*, 144 (2018) 1-11, Hefei, China, 8 December 2017. https://doi.org/10.1016/j.actaastro.2017.12.013

[7] Riggins, D., Tackett, T., Taylor, T., and Auslender, A., "Thermodynamic Analysis of Dual-Mode Scramjet Engine Operation and Performance," AIAA 2006-8059, *14th AIAA/AHI Space Planes and Hypersonic Systems and Technologies Conference*, 2006. https://doi.org/10.2514/6.2006-8059

[8] Chamberlain, B. L., "Additively-Manufactured Hybrid Rocket Consumable Structure for CubeSat Propulsion," Utah State University, Master's Thesis, 2018.

[9] Marshall, J. H., Whitmore, S. A., Heiner, M. C., "Thrust Augmented Nozzle for a Hybrid Rocket with a Helical Fuel Port," AIAA-2017-4983, *53rd AIAA/SAE/ASEE Joint Propulsion Conference*, Atlanta, GA, 10-11 July 2017. https://doi.org/10.2514/6.2017-4983

[10] Whitmore, S. A., Walker, S. D., Merkley, D. P., and Sobbi, M. "High Regression Rate Hybrid Rocket Fuel Grains with Helical Port Structures," *Journal of Propulsion and Power*, Vol. 31, No. 6 (2015), pp. 1727- 1738. http://dx.doi.org/10.2514/1.B35615

[11] Whitmore, S. A., Armstrong, I. W., Heiner, M. C., and Martinez, C. J., "High-Performing Hydrogen Peroxide Hybrid Rocket with 3-D Printed and Extruded ABS Fuel," A*eronautics and Aerospace Open Access Journal*, Vol. 2, No. 6, November, 2018. 10.15406/aaoaj.2018.02.00069.

[12] Whitmore, S. A., Inkley, *N. R.*, Merkley, D. P., and Judson, M. I., "Development of a Power- Efficient, Restart-Capable Arc Ignitor for Hybrid Rockets," *Journal of Propulsion and Power*, Vol. 31, No. 6 (2015), pp. 1739-1749. http://dx.doi.org/10.2514/1.B35595

[13] Whitmore, S. A., Peterson, Z. W., and Eilers, S. D., "Comparing Hydroxyl Terminated Polybutadiene and Acrylonitrile Butadiene Styrene as Hybrid Rocket Fuels," *Journal of Propulsion and Power*, Vol. 29, No. 3, 2013, pp. 582-592. https://doi.org/10.2514/1.B34382

[14] Constantine, M. T., and Cain, E. F., "Hydrogen Peroxide Handbook," AFRPL-TR-67-144, Edwards AFB CA, July 1967. https://www.researchgate.net/publication/235096265_Hydrogen_Peroxide_Handbook

[15] Whitmore, S., A., "Direct Ignition of a High Performance Hydrogen Peroxide Hybrid Rocket with 3-D Printed Fuel," *International Journal of Astronautics and Aeronautical Engineering*, Vol. 4, No. 21, 2019, ISSN 2631-5009, https://www.vibgyorpublishers.org/content/ijaae/fulltext.php?aid=ijaae-4-021.

[16] Gordon, S., and McBride, B. J., "Computer Program for Calculation of Complex Chemical Equilibrium Compositions and Applications," NASA RP-1311, 1994. https://www.grc.nasa.gov/www/CEAWeb/RP-1311.pdf

[17] Shapiro, A. H., *The Dynamics and Thermodynamics of Compressible Fluid Flow*, Wiley, New York, 1953, pp. 219-228. ISBN 0 471 06691-5.

[18] Miller, R. S., Harstad, K., Bellan, J., "Evaluation of Equilibrium and Non-Equilibrium Evaporation Models for Many-Droplet Gas-Liquid Flow Simulations," *International Journal of Multiphase Flow*, Vol. 24, No. 6, September 1998, pp. 1025-1055. https://www.sciencedirect.com/science/article/pii/S0301932298000287

[19] Ren, Z., Wang, B., Xie, Q., Wang, D., "Thermal Auto-Ignition in High-Speed Droplet-Laden Mixing Layers," *Fuel*, Vol. 191, March 2017, pp. 176-189. https://www.sciencedirect.com/science/article/pii/S0016236116311747

[20] Clift, R., Grace, J. R., Weber, M. E., *Bubbles, Drops, and Particles*, Academic Press, New York, 1978, p. 111. ISBN 0-12-176950-X.

[21] Ranz, W. E., and Marshall, W. R., Jr., "Evaporation from Droplets," *Chemical Engineering Progress,* Vol. 48, No. 3, March 1952, pp 141-146. http://dns2.asia.edu.tw/~ysho/YSHO-English/1000 CE/PDF/Che Eng Pro48, 141.pdf

[22] Poling, B. E., Prausnitz, J. M., O'Connell, J. P. *The Properties of Gases and Liquids*, 5th Edition, McGraw-Hill, New York, 2001, p. 11.5-11.7. ISBN 0-07-011682-2.

[23] Corpening, J. H., Heister, S. D., Anderson, W. E., "Thermal Decomposition of Hydrogen Peroxide, Part 2: Modeling Studies," *Journal of Propulsion and Power*, Vol. 22, No. 5, September 2006, pp. 996-1005. https://arc.aiaa.org/doi/abs/10.2514/1.13285?journalCode=jpp

[24] Anderson, J. D., *Modern Compressible Flow*, 3rd Edition, McGraw Hill, New York, 2003, pp. 108,191-234,377-403. ISBN-13: 978-0072424430. https://libcat.lib.usu.edu/search/i0070016542

[25] Whitmore, S. A., Martinez, C. J., Merkley, D. P., "Catalyst development for an arc-ignited hydrogen peroxide/ABS hybrid rocket system," *Aeronautics and Aerospace Open Access Journal*, Vol 2, No. 6, 2018. https://medcraveonline.com/AAOAJ/AAOAJ-02-00069.pdf

[26] Rarata, G., and Pawel, S., "The Safe Preparation of HTP and Concentrated H2O2 Samples," *Transactions of the Institute of Aviation*, Vol. 217, No 1, pp. 116-124, ISSN0509-669.

[27] Yansensky, D., Larson, C., Reali, J., Carl, C., "Citric Acid Passivation of Stainless Steel," *Aircraft Airworthiness and Sustainment Conference*, 19 April, 2011. https://ntrs.nasa.gov/archive/nasa/casi.ntrs.nasa.gov/20110001362.pdf

[28] Anthoine, J., Lestrade, J. Y., Messineo, J. "Performances of a Multi-Pulsed Hybrid Rocket Engine Operating with Highly Concentrated Hydrogen Peroxide," *53rd AIAA/SAE/ASEE Joint Propulsion Conference, Atlanta, GA*, 10-12 July 2017.

[29] Turns, S. R., *An Introduction to Combustion*, McGraw-Hill Higher Education Singapore, 2000, p. 376.

[30] Ronningen, J. E., Husdal, J. "Nammo Hybrid Rocket Propulsion TRL Improvement Program," *48th AIAA/SAE/ASEE Joint Propulsion Conference, Atlanta, GA*, 30 July-01 Aug 2012.

[31] Billig, F. S., "Design of Supersonic Combustors Based on Pressure-Area Fields," *Symposium (International) on Combustion*, Vol. 11, No. 1, 1967.